Monte Carlo Framework for Prostate Cancer Correction and Reconstruction in Endorectal Multi-parametric MRI

by

Dorothy Lui

A thesis
presented to the University of Waterloo
in fulfillment of the
thesis requirement for the degree of
Master of Applied Science
in
Systems Design Engineering

Waterloo, Ontario, Canada, 2014

This thesis consists of material all of which I authored or co-authored: see Statement of Contributions included in the thesis. This is a true copy of the thesis, including any required final revisions, as accepted by my examiners.

I understand that my thesis may be made electronically available to the public.

Statement of Contributions

Papers included in this thesis

D. Lui, A. Modhafar, J. Glaister, A. Wong, and M. Haider, "Monte Carlo bias field correction in endorectal diffusion imaging," *IEEE Transactions on Biomedical Engineering*, vol. 61, no. 2, pp. 368–380, Feb 2014.

This paper is incorporated in Chapter 3 of this thesis.

Contributor	Statement of contribution
Lui, D. (Candidate)	Conceptual design (70%) Data collection and analysis (70%) Writing and editing (50%)
Modhafar, A.	Conceptual design (10%) Data collection (10%) Writing and editing (10%)
Glaister, J.	Writing and editing (10%)
Wong, A.	Conceptual design (20%) Data collection and analysis (10%) Writing and editing (20%)
Haider, M.A.	Data collection (10%) Writing and editing (10%)

Abstract

Prostate cancer is one of the leading causes of cancer death in the male population. The detection of prostate cancer using imaging has been challenging until recently. Multi-parametric MRI has been shown to allow accurate localization of the cancers and can help direct biopsies to cancer foci which is required to plan treatment. The interpretation of MRI, however, requires a high level of expertise and review of large multi-parametric data sets. An endorectal receiver coil is often used to improve signal-to-noise ratio (SNR) and aid in detection of smaller cancer foci. Despite increased SNR, intensity bias fields can exist where nearest the endorectal coil the signal is greater than those regions farther from the coil. Weak delineation of the prostate as well as poor prostate gland visualization can greatly impact the ease and accuracy of diagnosis. For this reason, there is a need for an automated system which can correct endorectal multi-parametric MRI for enhanced visualization. A framework using Monte Carlo sampling techniques has been developed for prostate cancer correction and reconstruction in endorectal multi-parametric MRI. Its performance against state-of-the-art approaches demonstrate improved results for visualization and prostate delineation.

The first step in the proposed framework involves reconstructing an intensity bias-free image. Using importance-weighted Monte Carlo sampling, the intensity bias field is estimated to approximate the bias-free result. However, the reconstruction is still pervaded by noise which becomes amplified and non-stationary as a result of intensity bias correction. The second step in the framework applies a spatially-adaptive Rician distributed Monte Carlo sampling approach while accounting for the endorectal coil's underlying SNR characteristics.

To evaluate the framework, the individual steps are compared against state-of-the-art approaches using phantoms and real patient data to quantify visualization improvement. The intensity bias correction technique is critiqued based on detail preservation and delineation of the prostate from the background as well as improvement in tumor identification. The noise compensation approach is considered based on the noise suppression, contrast of tissue as well as preservation of details and texture. Utilizing quantitative and qualitative metrics in addition to visual analysis, the experimental results demonstrated that the proposed framework allows for improved visualization, with increased delineation of the prostate and preservation of tissue textures and details. This allows radiologists to more easily identify characteristics of cancerous and healthy tissue leading to more accurate and confident diagnoses.

Acknowledgements

Thank you to my supervisor Prof. Alexander Wong who has been a true mentor, motivator and inspiration during my Masters program. His guidance and support throughout my program showed me research in a new light and helped prove to myself my capacity and potential.

I would also like to thank Prof. David Clausi and Prof. Andrea Scott for reviewing my thesis. Taking the time out of your busy schedules to read and revise my thesis is greatly appreciated.

Thanks also to the colourful group of researchers in the Vision and Image Processing Research Lab who have made collaborations worthwhile and exciting. You have demonstrated to me that research can make leaps and bounds when great minds are put together. Also, thank you to the VIP Lab directors who have fostered a unique research environment where collaborations are possible and the norm. My research experience would not have been as diverse and engaging otherwise.

Finally, I want to show my appreciation to the Natural Sciences and Engineering Research Council (NSERC) of Canada for funding my work on this project.

Dedication

This thesis is dedicated to my family, friends and professors who have supported me throughout my endeavors. Without you all, this could not have been possible.

Table of Contents

List of Tables

List of Figures

Nomenclature

$\bar{A}, \bar{B}$	Means of two images used to calculate the correlation coefficient
$\bar{x}$	Mean intensity of a region
β	Background class for measuring probability of error
$\delta()$	Dirac delta function
η	Search space of voxels within a surrounding region of a voxel of interest
$\frac{n(s)}{\hat{b}_f(s)}$	Non-stationary noise
$\gamma(\theta)$	SNR profile characteristic of the endorectal coil
$\hat{C}_v$	Coefficient of variation is a scalar value which quantitatively assesses the intensity variation within a given region
$\hat{f}$	Bias field estimate
$\hat{w}$	Bias corrected estimate of the magnitude MRI
$\hat{\nu}(s_0)$	Estimated skew of the Rician distribution for the voxel of interest, s_0
$\hat{\Phi}(s_0)$	Estimated scale of the Rician distribution for the voxel of interest, s_0
$\hat{g}$	Noise-compensated reconstruction
κ	Desired number of samples to be selected from the search space
λ	Normalization term that allows the acceptance probability to equal 1 if s_k's neighbours are identical to those of s_0

$\mathfrak{L}$	Discrete lattice defining the endorectal prostate MRI image
Ω	Set of samples and associated importance weights
ω	Scaling factor of Butterworth model $t_1(s)$
ρ	Prostate class for measuring probability of error
σ	Parameter which controls the shape of the exponential and is based on the uncorrected log image
σ_b^2	Class variances for the surrounding background
σ_p^2	Class variance for the prostate gland
σ_r	Standard deviation of a given region
θ	Parameters to be estimated in maximum likelihood estimation
φ	Scaling factor of exponential model $f_2(s)$
ϖ	Class mean for the surrounding background
ϱ	Class mean for the prostate gland
ζ	Flatness of the Butterworth model
b	B-value for diffusion weighted magnetic resonance imaging which controls the sensitivity of the scan to diffusion
$D(s)$	Elliptical distance map approximating the endorectal coil SNR profile
D_0	Slope of the Butterworth model
F	Random field on S representing the bias field
f	Realization of F
G	Random field on S representing the noise and bias-free image
g	Realization of G
$h_k[j], h_0[j]$	j^{th} sites in the neighbourhoods around s_k and s_0
i, j	Describes the image dimensions

J	Fisher criterion value used to quantify the separability between two classes
N	Random field on N representing the noise process
n	Realization of N
$P(\epsilon)$	Probability of error
P, Q	Two images used to calculate the correlation coefficient
r	Correlation coefficient describes how dependent two images are with one another
S	Set of voxels on a discrete lattice $\mathfrak{L}$
s	Voxel in $\mathfrak{L}$ such that $s \in S$
s_0	Voxel of interest
S_b	Computed DWI with b-value b
s_k	Subset of voxels
$t_1(s)$	Butterworth model
$t_2(s)$	Exponential model
u	Random value that is drawn from a uniform distribution
V	Random field on S representing the acquired image
v	Realization of V
W	Random field on S representing the bias-free image
w	Realization of w
x	Observed intensities in the noise-compensated reconstruction $\hat{g}(s)$

Chapter 1

Introduction

Prostate cancer is the uncontrolled cellular growth of the prostate; an organ in the male reproductive system that is responsible for secreting a nutrient-filled fluid that constitutes the majority of semen [1]. Cancer in the prostate results in abnormal prostate structure and can impact urinary and erectile function. Unfortunately, prostate cancer is the most commonly diagnosed form of cancer in the United States and Canada, encompassing 14 and 24% of all new cancer cases respectively. In 2014, it was estimated that $233,000$ American and $23,600$ Canadian men would be diagnosed with prostate cancer and of those cases, $29,480$ and $4,000$ were expected to result in death [2, 3]. With these staggering statistics, it is important towards patient survival to obtain treatment during the early stages of the cancer before it metastasizes to surrounding tissues [1, 4]. Furthermore, in the late stages of prostate cancer, there is poor prognosis [5] encouraging early and accurate detection approaches. The accuracy of detection approaches is also critical since treatment of prostate cancer with radiation or surgery carries significant risk of life altering side effects such as sexual dysfunction, urinary and rectal incontinence and thus should not be undertaken unless necessary [5–7].

1.1 Current cancer screening approaches

Presently, prostate cancer can be detected using a variety of tests. The prostate-specific antigens (PSA) test is a commonly used blood test which measures the levels of the PSA or toxins uniquely related to the prostate. High levels of PSA indicate high prostate cancer risk. Its use, however, is controversial and often inadequate as it over-detects clinically insignificant prostate cancer, resulting in a high degree of over-treatment. Moreover, other

prostate-unrelated factors can cause the rise of PSA levels and disagreement over threshold PSA levels have also increased the number of false positives [5–7]. Alternatively, a digital rectal examination can be exercised where a doctor feels the prostate through the rectum for signs of hard lumps, indicative of tumors. This detection approach is useful for detecting only common areas where prostate cancer is found and requires further testing. Moreover, a digital rectal examination is uncomfortable and invasive. Another commonly used detection approach is transrectal ultrasound (TRUS). TRUS is an imaging approach where ultrasound is used to image the prostate. The technique involves inserting a small probe into the rectum to project sound waves through the rectum and to the prostate gland and then record the echoes. Tumorous regions have differing echo responses from healthy tissue though further analysis via biopsy is required. Prostate tumors imaged using TRUS have also been found to appear isoechoic and difficult to differentiate from surrounding tissue [8].

Following the previous initial tests for screening, if the tests come back positive for prostate cancer the next step is systematic TRUS-guided biopsy. This involves regional sampling of the prostate with typically eight or more samples collected [7]. This is even more invasive and uncomfortable, and suffers from sampling error due to the isoechoic nature of prostate tumors when imaged using TRUS. As such, to consider detection alternatives is important.

1.2 MRI for prostate cancer screening

The detection approaches described previously in Section 1.1 each have their drawbacks, whether due to accuracy, inability to access or visualize certain prostate locations, or requiring invasive action. The use of magnetic resonance imaging (MRI) has shown to be a viable alternative as it can visualize the cancer and has a good negative predictive value for significant cancer, helping avoid unnecessary biopsy and reduction of sampling error [7].

MRI is a form of imaging used in radiology to visualize the body in a tomographic view, where thin sections are imaged to obtain two-dimensional images or slices and repeated for the entire body to form a volume. For acquisition, the patient is placed in a large magnet that generates a large magnetic field. The magnetic field aligns atomic nuclei in the body to produce faint signals which are then detected and collected to form high contrast images of soft tissue. For prostate cancer, MRI has become a commonly used diagnostic imaging tool for detection due to its improved contrast between cancer and background healthy tissue [7]. In particular, multi-parametric MRI has been found useful for visualizing prostate cancer and its definition and advantages are introduced in Section 1.3.

1.3 Multi-parametric MRI

Within MRI, there are a variety of MRI techniques available which highlight different tissue details. Combining multiple MRI techniques is called multi-parametric MRI, where changing the imaging parameters results in the emphasis of specific features. One type of MRI called T2-weighted MRI can be used to focus on fluids in tissue. These images are recognized as a strong candidate for diagnostic prostate cancer analysis [9,10] as they improve soft tissue contrast in comparison to other modalities or imaging techniques. However, it has been reported that tumors occurring on the central gland cannot be distinguished from other low-signal intensity deformations that result from non-cancerous situations [11,12]. Furthermore, the use of T2-weighted MRI requires highly-qualified sub-specialty radiologists to interpret MRI data due to the subtle delineation between cancerous and healthy tissue [4]. As a result, improving T2-weighted MRI images for analysis as well as using multi-parametric MRI can help radiologists more easily analyze and detect prostate cancer.

Another promising modality currently under investigation for prostate cancer diagnosis is diffusion-weighted MRI (DWI), which is sensitive to diffusion processes in biological tissues due to random thermal flow of water molecules [11–13]. Prostate cancerous tissue has high-cellular density which results in the restricted diffusion of water. As such, diffusion-weighted imaging can capture various molecular properties in different parametric settings, which leads to high contrast between healthy and cancerous tissue [11,13,14]. In particular, one parameter called the b-value controls the sensitivity of the scan to diffusion and increasing its value (e.g., b-values greater than 1,000 s/mm^2) has been found to provide improved delineation between tumors and benign tissues [15–18] making it a very promising tool for prostate cancer detection and localization [4].

The particular combination of T2-weighted MRI with DWI has been shown to have higher sensitivity for detecting prostate cancer [19]. Improving the SNR in the prostate region further can also be beneficial in differentiating between healthy and cancerous tissues. The use of surface and endorectal coils for this purpose is discussed in more detail in Section 1.4.

1.4 Surface and endorectal coils

Signal-to-noise ratio (SNR) improvement within the prostate can be achieved by introducing loops of conductive wire to increase magnetic sensitivity in specific regions. These loops are called receiver coils and act as an antenna to improve the signal for clearer images in the

region of interest. For prostate MRI, a localized surface receiver coil is sometimes placed directly on the skin's surface over the pelvic region with some coils specifically designed for this region, conforming to this part of the body. An example of a surface coil is shown in the left image of Figure 1.1. This method, however, finds the coil relatively far from the centrally located prostate (i.e., > 10 cm) and as a result does not introduce significant SNR improvements.

(a) Surface Receiver Coil[1] **(b)** Endorectal Coil[2]

Figure 1.1. Left: A man fitted with a surface receiver coil to improve the SNR in the pelvic region for enhanced prostate visualization. Right: An endorectal coil

For closer proximity to the prostate, receiver coils covered with a latex balloon, called endorectal coils (ERCs) are used. ERCs are placed in the rectum, or the last segment of the large intestine which sits inside the pelvis directly behind the prostate gland. Thus, in the rectum, the coil is within a few millimeters of the prostate gland. This allows for more detailed imaging of the prostate and surrounding tissue. More recently, ERCs have been shown to offer a diagnostic advantage [20] in the detection of prostate cancer compared to surface coils at 3 T. As such, there remains a strong interest in utilizing ERC despite the discomfort associated with insertion of the endorectal balloon. For lower field systems operating at 1.5 T, ERC is helpful in achieving performance similar to 3 T MRI with pelvic phased-array coils (PAC) [21, 22]. The results demonstrated no significant visualization difference between the two approaches, although according to Beyersdorff *et al.* [22] ERC exhibited improved SNR. Thus, the use of endorectal coils remains a particular interest at 1.5 T as well where stronger magnetic field MRI scanners are not readily available.

[1] www.healthcare.siemens.co.uk/magnetic-resonance-imaging/mri-guided-therapy/magnetom-combi-suite/use

[2] www.medrad.com/en-us/info/products/Pages/ColorectaleCoil.aspx

For closer proximity to the prostate, receiver coils covered with a latex balloon, called endorectal coils (ERCs) are used. ERCs are placed in the rectum, or the last segment of the large intestine which sits inside the pelvis directly behind the prostate gland. Thus, in the rectum, the coil is within a few millimeters of the prostate gland. This allows for more detailed imaging of the prostate and surrounding tissue. More recently, ERCs have been shown to offer a diagnostic advantage [20] in the detection of prostate cancer compared to surface coils at 3 T. As such, there remains a strong interest in utilizing ERC despite the discomfort associated with insertion of the endorectal balloon. For lower field systems operating at 1.5 T, ERC is helpful in achieving performance similar to 3 T MRI with pelvic phased-array coils (PAC) [21, 22]. The results demonstrated no significant visualization difference between the two approaches, although according to Beyersdorff *et al.* [22] ERC exhibited improved SNR. Thus, the use of endorectal coils remains a particular interest at 1.5 T as well where stronger magnetic field MRI scanners are not readily available.

Appropriately, developing a framework to enhance the visualization of endorectal prostate imaging in T2-weighted MRI and DWI for prostate cancer analysis is beneficial to radiologists. As a consequence of considering multi-parametric MRI, however, there are a number of inherent challenges which will be discussed in more detail in the following section (Section 1.5).

1.5 Challenges

The use of endorectal multi-parametric MRI, although strongly motivated, suffers from fundamental challenges which need to be addressed. In this section, the obstacles intrinsic to using endorectal coils with T2-weighted MRI and DWI are discussed. Although ERCs improve SNR in the prostate gland, their use introduces a challenge called intensity bias. A secondary challenge results from using coil intensity correction techniques built into MRI scanners to account for intensity bias which leads to noise variation and amplification. These inter-related obstacles are depicted in more detail in the following sections.

1.5.1 Intensity bias in endorectal multi-parametric MRI

When imaging the prostate, better SNR can be achieved using a localized surface receiver coil or an endorectal coil (ERC). With both surface and endorectal coils, the signal decreases farther away from the coil and consequently introduces intensity inhomogeneities. In the case of ERCs, due to physiological limitations, these coils are designed to be small,

which causes inhomogeneous signal distribution [7]. As a result, the intensity bias can cause difficulties visualizing regions in the prostate farther from the ERC while regions closest to the coil can appear brighter. This impacts the delineation of the prostate and visualization for diagnosis. In the case of DWI, bright regions could be a result of the intensity bias or due to cancerous regions, increasing the necessity for an intensity bias correction approach. Examples of intensity bias in DWI and T2-weighted MRI are shown in Figure 1.2, where the red arrows indicate regions with increased intensity and the blue arrows specify regions with decreased signal due to distance from the ERC. The poor delineation of the prostate from the background as well as the poor visualization of the regions farther away from the ERC motivate the necessity for an intensity bias correction approach for multi-parametric MRI.

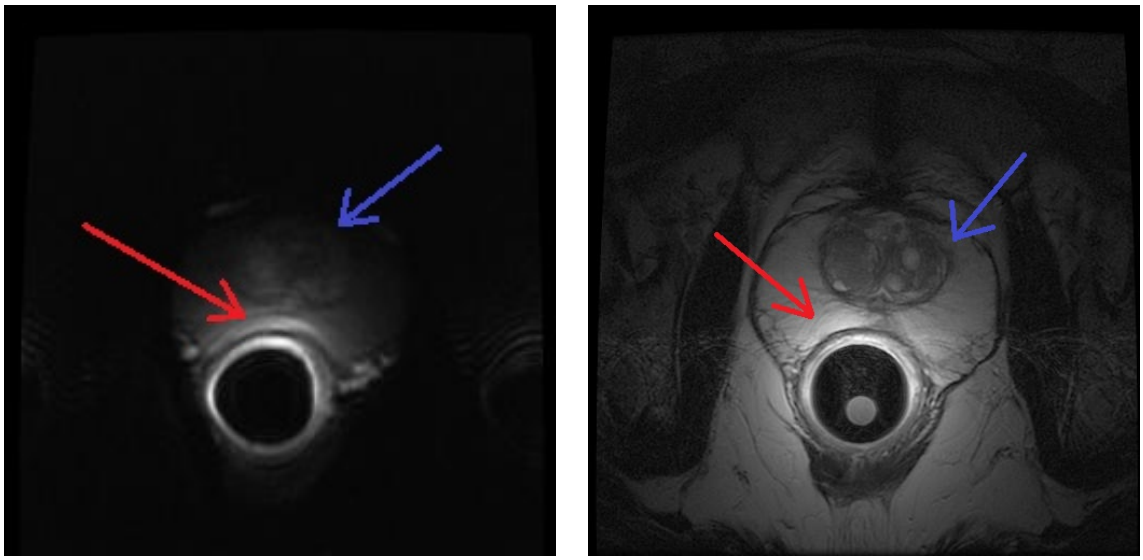

(a) DWI **(b)** T2-weighted MRI

Figure 1.2. DWI and T2-weighted MRI examples of intensity bias in the prostate gland. Red arrows indicate increased intensity regions while blue arrows specify decreased intensity areas which are farther from the endorectal coil.

1.5.2 Noise variation and amplification in coil intensity corrected endorectal multi-parametric MRI

The intensity bias caused by ERCs in MRI can be corrected using built-in MRI pre-calibration correction approaches. One of the consequences of using such intensity correction approaches is that it creates a spatial dependence on background point noise (which is uniformly dispersed [23, 24] prior to correction). This results in increasing noise levels as we move away from the coil in the corrected images, which is particularly visible in regions distant from the coil [23]. An example is shown in Figure 1.3 where a T2-weighted MRI image without correction is compared with the same image with the correction. In the image without correction, the intensity bias is more prevalent nearest the ERC and the regions farther away from the ERC suffer from low SNR. In the corrected image, the previously low SNR regions are now more visible and the delineation between regions have improved. However, the noise in these areas have also become intensified as a result of the pre-calibrated intensity bias correction approach [7].

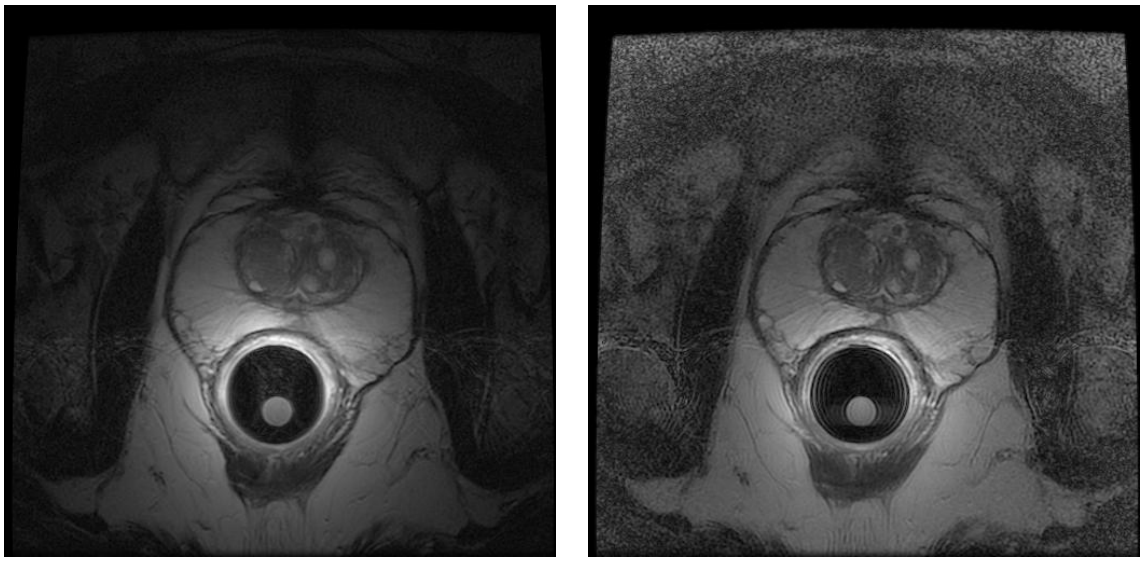

(a) T2-weighted MRI with no correction

(b) T2-weighted MRI with pre-calibrated intensity bias correction

Figure 1.3. An example of a T2-weighted MRI slice demonstrating the intensity bias (left) without any correction and the consequent noise variation and amplification caused by the pre-calibrated intensity bias correction provided by the MRI scanner (right).

MRI noise, introduced by patient motion and electronic noise during acquisition is

an issue under active research [25, 26]. It amounts to difficult analysis and hinders post-processing approaches such as segmentation and registration [26, 27]. Raw MRI data is complex (both real and imaginary components) and represented in the frequency domain with additive Gaussian noise. Transforming this complex data to the spatial domain renders the magnitude data to be Rician distributed [26, 28, 29]. The data distribution is also dependent upon the SNR, where low SNR regions (mainly described by noise only) can be alternatively modeled as Rayleigh distributed [29, 30] and high SNR regions as Gaussian distributed [26, 29, 31]. Moreover, the signal-dependent nature of noise in the intensity corrected images introduces challenges to noise compensation and further complicates its removal by introducing a signal-dependent bias to the MRI intensities [26, 31]. The bias has been accounted by applying correction in the squared magnitude domain whereby the Rician distribution becomes non-central Chi-square distributed [26, 32]. Taking the characteristic distributions of MRI data into consideration, noise compensation can be completed for improved visualization and analysis of the prostate in intensity corrected endorectal MRI.

Recognizing these challenges, there is a need to correct for the intensity bias that results from using endorectal coils in MRI and a noise compensation approach for intensity bias corrected MRI. In this thesis, a Monte Carlo framework to address these challenges for enhanced visualization and analysis is presented.

1.6 Proposed solution and thesis contributions

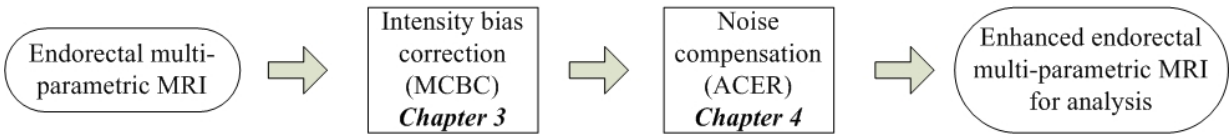

Figure 1.4. Flow chart describing the proposed Monte Carlo framework for improving endorectal multi-parametric MRI for prostate cancer visualization and analysis.

The purpose of this thesis is to propose a Monte Carlo framework for improving the visualization and analysis of the prostate for diagnosing prostate cancer in endorectal multi-parametric MRI. There are two main contributions:

1. An intensity bias correction approach for endorectal MRI which develops a bias field estimate through non-parametric modeling based on the Monte Carlo sampling approach is presented in Chapter 3. The estimate is formulated to remove the intensity

inhomogeneity from the acquired image to improve subsequent segmentation and diagnosis. This technique is called Monte Carlo bias correction (MCBC) [4].

2. A new approach called adaptive coil enhancement reconstruction (ACER) which compensates for the noise in intensity bias corrected endorectal MRI. The approach considers the underlying Rician distribution of the data as well as the inherent ERC SNR profile used. The formulation, implementation and test results are found in Chapter 4 [7].

The two main contributions focus on enhancing the visualization and delineation of the prostate in DWI and T2-weighted MRI respectively to facilitate analysis for prostate cancer (shown in Figure 1.4). In this thesis, a review of relevant state-of-the-art methods are presented in Chapter 2. Problem formulation and test results against other state-of-the-art approaches are included for each of the two main contributions in Chapters 3 and 4. Finally, in Chapter 5, conclusions and future extensions are discussed.

Chapter 2

Background

In this section, the related works for each proposed contribution are presented. A brief description of the existing types of approaches and their limitations are discussed to lead into the algorithms within the proposed framework. The relevant work for intensity bias correction in MRI is weighed in Section 2.1 with the applicable literature for noise compensation in MRI investigated in Section 2.2.

2.1 Intensity bias correction in endorectal MRI

In Section 1.5.1, intensity bias was presented as an inherent challenge of using endorectal coils. The approaches proposed for intensity bias correction can be divided into two types: prospective and retrospective. Prospective methods include techniques which account for the intensity bias prior to acquisition while retrospective approaches involve post-processing of the acquired images to remove the intensity bias. The related work discussed in this section are separated into these two categories in Section 2.1.1 and 2.1.2.

2.1.1 Prospective approaches

To overcome intensity bias, prospective approaches aim to adjust for the bias prior to imaging, under the assumption that the bias results from the MRI acquisition process. One approach is to image a homogeneous phantom to estimate the intensity bias field and consequently divide this bias from the acquired image of the desired object. This approach, however, does not account for bias fields that result from the patient's anatomy [33].

Moreover the location of the coil needs to be consistent between the acquisitions of the phantom and the patient. The inflexibility of this approach based on the fact that the bias field estimate is generated on a single set of imaging parameters makes this approach undesirable [34–36].

Other prospective approaches come built into the MRI scanner. A common feature is the surface coil intensity correction (SCIC) algorithm [23, 34, 37] that employs low-pass filtered, shrunken and thresholded versions of the signal to form an estimate of the bias field. The uncorrected image is then divided by the estimated bias. An alternative technique is using pre-calibration through a series of proton-density (PD) weighted images to determine the bias profile. Then a correction matrix can be generated and applied to correct upon future acquisitions [38]. This approach has been realized in commercial systems such as Phased array UnifoRmity Enhancement (PURE - General Electric (GE)), Prescan Normalize (Siemens), CLEAR (Philips) and NATURAL (Hitachi) [7]. Also accessible in some MRI scanners, this correction process is time consuming, increasing the acquisition time due to the additional PD weighted images. Additional acquisition time causes the scan to be more susceptible to motion artifacts. Moreover, noise amplification in regions with low SNR ensues leading to poor visualization. In the second contribution of this thesis, this particular challenge is addressed (Chapter 4).

2.1.2 Retrospective approaches

In the second category of intensity bias correction approaches, post-processing techniques of acquired images can be categorized as: filtering [39, 40], surface fitting [41, 42], segmentation-based approaches [43, 44] and statistical approaches [45–47]. These approaches aim to correct for the intensity bias using a more generalized approach by making fewer assumptions and can be used to correct for intensity bias not caused by MRI scanners.

Filtering

The simplest type of correction are filtering approaches which infer the bias field as a low-frequency artifact. As such, using a low-pass filter can retain the details in the higher frequencies. The results, however, prove that this assumption is valid only for small structures and instead can introduce edge artifacts, overcompensation in homogeneous tissues and removal of fine details and texture [35, 36]. Averaging and median filters have also been employed to isolate small intensity variation regions which are then smoothed using a Gaussian filter [39]. Zhou *et al.* [40] also used average filtering of the image combined with the original image to approximate the bias field.

Another popular form of filtering proposed are homomorphic filters which remove the low-frequency bias field using a low-pass filter on the log transform of the image [33]. The intent of using these filters is to improve image contrast and normalize the intensity of the data [36]. Although simple and fast to implement, in some cases it can distort tissue intensity values and add artifacts to corrected images [33, 41, 48].

Surface fitting

Surface fitting methods fit a parametric surface to a set of image features that contain information on the intensity inhomogeneity. A polynomial or spline-based surface is derived to estimate the bias field of the input image and bases the surface on the intensities within the image. Following surface fitting, the original image is divided by the computed bias field or surface. For polynomial or spline-basis surfaces, fitting can be accomplished using the manual or automatic selection of control points to dominant tissue. It can also be implemented through minimization of an energy function [41]. The drawback to surface fitting techniques are that the surface corrects for major tissue and then extrapolates for surrounding areas assuming the corrections are applicable to other tissue types in the image [35, 48]. Moreover, the manual selection of points is subjective and time-consuming depending on optimization processes [49].

Another surface fitting approach is to use intensity inhomogeneity gradients to extract homogeneous regions. The homogeneous regions are then intensity normalized for surface fitting and the surfaces used to model the bias field. The assumption is that all pixels within these homogeneous regions are distorted with the same bias although this is unlikely to be the case. Additionally, undesired details can be included into the bias estimate during extraction of the homogeneous areas and cause them to consequently be removed [36, 42].

Segmentation-based approaches

An alternative approach to intensity bias correction is segmentation. In many cases, removing the bias field is a pre-processing step towards completing the segmentation of interest regions, however, in these intensity bias correction approaches, inhomogeneity removal and segmentation are combined simultaneously. A clustering approach called fuzzy C-means (FCM) proposed for segmentation in MRI was adapted to accommodate clustering to local variations to allow for more accurate classification of soft tissues versus outliers [43].The segmented soft tissue is then corrected using a low-pass local means filtering approach to estimate the bias field. Another approach suggested an adaptive FCM approach which

considers the class centroid as a function of location [44]. Yet FCM techniques assume that image voxels belong to more than one class, introducing complex and time-consuming iterative routines [35]. Moreover, the use of segmentation to correct for the bias field generates a circular problem where the accuracies of both segmentation and the existing bias field depend on each other [50]. As a result of the present bias field, poor segmentation ensues and leads to a poor extraction of the bias field region and causes overcompensation in regions not affected by the bias field.

Statistical approaches

The last group of intensity bias correction approaches considered are statistical methods. This group of techniques use the maximum-likelihood or maximum a posteriori probabilities to estimate the intensity probability distribution within the data [35, 36]. By labeling pixels based on their underlying statistical probability characteristics, the data is essentially being clustered or segmented. This makes the assumption that the inhomogeneity in the image follows a predictable distribution which is often not the case [50]. Using finite mixture and finite Gaussian mixture models, a criterion for classification is found [45, 46], however, without consideration of spatial location [36]. By assuming a parametric model that may not accurately model the intensity bias field, the correction can suffer. One approach forgoes assuming a parametric model and instead estimates the bias field via a complete space search of all possible bias-free distributions [47]. Yet the space of all bias-free distributions can be an exhaustive search as well as performance-dependent upon what distribution is selected [4].

2.2 Noise compensation for coil intensity corrected MRI

Following intensity bias correction, noise can become amplified and as a result influence the visualization and analysis of the prostate in MRI. Various noise compensation approaches have been proposed for MRI and utilize different strategies for noise suppression. The strategies implemented are depicted in Section 2.2.1 with the assorted methods for noise compensation in MRI described in Section 2.2.2.

2.2.1 Strategies for noise compensation in MRI

The strategies for noise compensation in MRI attempt to harness the underlying properties of noise in MRI. One strategy is to consider the use of spatial adaptation to the noise variance. By employing the ERC, signal varies spatially and as a result the noise variance is dependent upon location. Regions closest to the ERC have higher signal and lower noise variance while areas farther from the coil have lower signal and higher noise variance. In cases where algorithms do not take spatial location into account, overcompensation of noise can occur, either leading to undersuppression of noise or oversuppression. A number of proposed algorithms [25,32,51–53] have taken this into consideration. A second tactic in addressing MRI noise is to recognize the underlying probabilistic distribution of the data. Following reconstruction, the magnitude data becomes Rician distributed. Acknowledging the data's fundamental Rician nature allows for improved noise modeling for enhanced compensation of noise. An assortment of methods have taken this under deliberation [32, 51–57]. Finally, noise in MRI data causes a bias in the data's intensities which is addressed by many approaches [25, 52–55, 57]. The various approaches for noise compensation in MRI make use of these strategies and are described in more detail in the following section (Section 2.2.2).

2.2.2 Noise compensation techniques in MRI

Numerous approaches have been proposed using MRI magnitude data to compensate for noise, using a variety of methods including total variation [51, 56, 58], analyzing multiple scales using wavelet denoising [52,54,55,57], via non-local means [27,31,32,53], linear minimum mean-square error (LMMSE) estimators [26,59] and masks [34,60]. These approaches are interpreted in the following sections.

Total variation

The total variation (TV) approach is a popular nonlinear denoising technique which minimizes noise (variation) by minimizing the total variation of an image. This results in the removal of undesired noise while preserving edge features. Keeling *et al.* [58] introduced a TV approach which corrects for noise and the intensity bias introduced by a surface coil by minimizing the model residual. A common challenge with TV approaches is optimal parameter selection and is especially difficult in situations of varying noise levels [51]. Varghees *et al.* [51] proposed an adaptive regularization parameter which self-adjusted based on the noise standard deviation. These TV approaches, however, do not account for

the Rician-nature of MRI magnitude data which as described previously can be a useful strategy. Furthermore, TV methods have been found to be computationally inefficient and overcompensate for noise due to inaccurate regularization parameter selection due to approximations [56]. More recently, Martin *et al.* [56] introduced a TV approach which accounts for the Rician characteristics of MRI magnitude data in a new framework which allows for more accurate and efficient minimization.

Wavelet denoising

Wavelet denoising has also been applied for MRI denoising; decomposing the data into the multiscale wavelet domain. This decomposition allows features of interest to be preserved while removing undesired noisy signals by thresholding coefficients that define noise. Novak [57] adapted the wavelet-domain filter to adapt to the spatially-varying noise and the Rician nature of MRI magnitude data. Pizurica *et al.* [52] generalized this approach by developing a wavelet-domain filter which adapts to the various underlying noise distributions without relying on prior knowledge of the noise distribution. Wavelet-based bilateral filtering schemes have also been proposed [54, 55] to effectively represent noisy signals using an undecimated wavelet transform while bilateral filtering was applied for its efficiency and effective preservation of edge features. The limitation of a bilateral filtering approach is that these filters can overcompensate for noise in homogeneous regions. In the case of prostate MRI, important tissue textures need to be preserved for more detailed analysis. The limitation of wavelet denoising is the threshold selection as hard thresholding has been found to introduce discontinuities [51]. Moreover, wavelet denoising can introduce artifacts depending on the type of wavelet basis used [25].

Non-local means

Based on the spatial variation of MRI noise following surface coil intensity correction, another popular approach for denoising MRI are non-local means (NLM) approaches based on the algorithm proposed by Buades *et al.* [61]. These approaches [27, 31, 32, 53] exploit the redundant regions of an image for denoising. A weighted average of pixels in redundant regions is used to estimate the noise-free regions instead of local noise-compensating filters which only rely on the pixels in its neighbourhood. The noise suppression, however, is dependent upon finding similar regions that are corrupted by noise. As such, regions of high noise can introduce artifacts [62]. Nonetheless, this methodology has been adapted to MRI noise by considering the Rician distribution of MRI magnitude data, optimal parameter selection [27], inspired a non-local maximum likelihood estimation [32] and

accounted for signal bias [31]. Coupé *et al.* [53] also modified the NLM approach by presenting a multi-resolution approach which adapts denoising based on the spatial and frequency information.

Linear minimum mean-square error estimators

Linear minimum mean-square error (LMMSE) estimators are a set of estimation approaches which enforce a linear function estimator to minimize the mean-squared error of the measurements. Often these techniques require a compromise between optimization and complexity. Similar to NLM methods, however, LMMSE estimators have been adapted for MRI denoising [26, 59]. Aja-Fernández *et al.* [59] introduced an LMMSE for Rician-distributed MRI magnitude data, presenting four different approaches to estimate noise variance. This approach is limited to assuming a uniform background which makes this approach less suitable for prostate MRI. More recently, Golshan *et al.* [26] proposed LMMSE for three-dimensional MRI denoising, introducing a more efficient approach of sampling the MRI data for improved noise variance results.

Masking approaches

More specific to the challenge presented in this thesis of noise amplification are masking approaches developed to explicitly handle noise magnification caused by surface coil intensity correction. Axel *et al.* suggested a mask for removing the amplified noise [34]. A general mask, however, may not be suitable for all images and is time-consuming to obtain. Kellman *et al.*used normalization of high spatial resolution PD images in myocardial MRI and proposed a region filling approach using binary masks to remove the amplified noise [60]. Time consuming additional acquisition is undesirable for patient comfort and introduces risk of motion artifacts. A post-processing technique for treating noise amplification which does not require manual annotation or additional acquisitions is preferred.

2.3 Summary

Existing solutions were presented for intensity bias correction in endorectal MRI as well as noise compensation in coil intensity corrected MRI. For intensity bias correction, prospective methods use phantoms and pre-calibration acquisitions to correct the bias prior to imaging. These approaches increase acquisition time and fail to account for bias resulting from the patient's anatomy. Retrospective approaches complete post-processing of

MRI acquisitions using filtering, surface fitting, segmentation and statistical approaches. Parameter and manual point selection, introduction of artifacts and parametric model assumptions include some of the common challenges with the existing retrospective solutions. For noise compensation in coil intensity corrected MRI, utilizing the underlying characteristics of MRI data has allowed for improved correction using total variation, wavelet denoising, non-local means, linear minimum mean-square error estimators and masking. These solutions, however, suffer from issues such as parameter selection, detail preservation and introduction of artifacts. As such, there needs to be techniques which can retain the detail in the prostate while reducing noise and intensity bias which impact analysis and diagnosis.

In this thesis, a post-processing intensity bias correction approach is introduced which estimates the bias field through non-parametric modeling using a Monte Carlo sampling approach. The estimate is formulated to remove the intensity inhomogeneity from the acquired image, allowing for improved visualization and analysis. The method, called Monte Carlo bias correction (MCBC) is presented in Chapter 3. In addition, a novel noise-compensation reconstruction approach called adaptive coil enhancement reconstruction (ACER) is presented in Chapter 4. ACER reconstructs noise-compensated endorectal MR images using a stochastic Bayesian estimation framework. A spatially-adaptive Monte Carlo sampling approach is introduced to estimate the posterior distribution using a Rician model. The Monte Carlo posterior estimation is modified to model the Rician-nature of MRI magnitude data. Moreover, the SNR profile of the specific ERC used is incorporated into the posterior estimation by integrating a learned parametric non-stationary Rician model. The model is learned using maximum likelihood estimation based on the data and specifications of the ERC. The posterior estimate is then used to form a noise-suppressed reconstruction using Bayesian least-squares estimation while correcting for a Rician-induced intensity bias using a spatially-varying second-order moment [7].

Chapter 3

Intensity Bias Correction in Endorectal Multi-parametric MRI

In this chapter, a novel intensity bias correction approach is presented called Monte Carlo bias correction (MCBC) [4]. Using importance-weighted Monte Carlo sampling, an estimate of the intensity bias field is generated to approximate the bias-free result. The problem formulation and methodology are described in this chapter. Experimental tests utilizing phantoms and real patient data evaluate the performance of MCBC against five other state-of-the-art techniques used for intensity bias correction based on quantitative and qualitative analysis.

3.1 Problem formulation

In this section, the problem formulation and the methodology of how the non-parametric bias field is estimated is discussed. This is followed by an explanation of how the bias field estimation is applied to construct the corrected image.

The intensity inhomogeneity model can be modeled as a multiplicative relationship. Let S be a set of voxels on a discrete lattice $\mathfrak{L}$ defining the endorectal prostate MRI magnitude image, and let $s \in S$ be a voxel in $\mathfrak{L}$. Let the random fields on S, $V = \{V(s)|s \in S\}$ represent the acquired image, $W = \{W(s)|s \in S\}$ be the bias-free image and $G = \{G(s)|s \in S\}$ be the bias-free and noise-free image. Also, let $F = \{F(s)|s \in S\}$ be the bias field and $N = \{N(s)|s \in S\}$ be the noise process. Let $v = \{v(s)|s \in S\}$, $w = \{w(s)|s \in S\}$, $g = \{g(s)|s \in S\}$, $f = \{f(s)|s \in S\}$ and $n = \{n(s)|s \in S\}$ be

realizations of V, W, G, F and N respectively. The intensity inhomogeneity model for MRI can be modeled as a multiplicative relationship [35, 50], where $v(s)$ is

$$v(s) = g(s) \cdot f(s) + n(s) \tag{3.1}$$

Based on the model defined in Equation 3.1, the inverse problem of estimating the bias-free image $w(s)$ can be formulated as:

$$\begin{aligned} w(s) &= \frac{v(s)}{f(s)} \\ &= g(s) + \frac{n(s)}{f(s)}. \end{aligned} \tag{3.2}$$

By removing the bias field f from the acquired image v, the resulting additive noise process $\frac{n(s)}{f(s)}$ is spatially variant as a result of the bias field's inherent spatial variation. This is in contrast to the stationary noise process $n(s)$ which previously affected the acquired image. To handle this, a novel approach is presented in Chapter 4. In this chapter, the objective is to obtain an estimate of $w(s)$, denoted as $\hat{w}(s)$. To do this, the bias field estimate $\hat{f}$ can be formulated in logarithmic space given the acquired image v as the Bayesian least-squares estimation problem below:

$$\log(\hat{f}) = \underset{\log(\hat{f})}{\arg\min}\, E\left((\log(f) - \log(\hat{f}))^2 | \log(v)\right). \tag{3.3}$$

The Bayesian estimate in Equation 3.3 can then be expressed as the mean of the posterior distribution:

$$\log(\hat{f}) = \underset{\log(\hat{f})}{\arg\min}(\int (\log(f) - \log(\hat{f}))^2 p(log(f)|\log(v)) d(\log(f))). \tag{3.4}$$

Taking the derivative of Equation 3.4 with respect to $log(\hat{b})$ gives us

$$\begin{aligned}
&\frac{\partial}{\partial(log(\hat{f}))}\int(\log(f)-\log(\hat{f}))^2 p(\log(f)|\log(v))d(\log(f)) \\
&=\int -2(\log(f)-\log(\hat{f}))p(\log(f)|\log(v))d(\log(f)) \\
&=\int(-2\log(f)+2\log(\hat{f}))p(\log(f)|\log(v))d(\log(f)) \\
&=\int -2\log(f)p(\log(f)|\log(v))d(\log(f))+\int 2\log(\hat{f})p(\log(f)|\log(v))d(\log(f))
\end{aligned} \tag{3.5}$$

Then setting the derivative to zero, Equation 3.5 can be rearranged:

$$\begin{aligned}
&\int \log(f)p(\log(f)|\log(v))d(\log(f)) \\
&=\int \log(\hat{f})p(log(f)|log(v))d(log(f)).
\end{aligned} \tag{3.6}$$

Simplifying the right hand side of Equation 3.6,

$$\begin{aligned}
&\int \log(\hat{f})p(\log(f)|\log(v))d(\log(f)) \\
&=\log(\hat{f})\int p(\log(f)|\log(v))d(\log(f)) \\
&=\log(\hat{f}).
\end{aligned} \tag{3.7}$$

Therefore, Equation 3.7 becomes

$$\log(\hat{f})=\int \log(f)p(\log(f)|\log(v))d(\log(f)). \tag{3.8}$$

Thus, the bias field b may be estimated as:

$$\hat{f}=\exp\left(\int \log(f)p(\log(f)|\log(v))d(\log(f))\right). \tag{3.9}$$

Equation 3.9 implies that the bias field estimate requires the posterior distribution, $p(\log(f)|\log(v))$ (to be formulated in Equation 3.11), which can be complicated and difficult to obtain analytically. Therefore, a non-parametric approach is instead applied to estimate $p(\log(f)|\log(v))$ via importance-weighted Monte Carlo sampling [63].

3.2 Non-parametric posterior estimation

The importance-weighted Monte Carlo sampling approach [63] was employed to estimate $p(\log(f)|\log(v))$. This approach establishes Ω, a set of samples and associated importance weights from a search space of voxels, η, within a surrounding region of a voxel of interest, s_0. Then, an instrumental distribution, $Q(s_k|s_0)$, is used to randomly select a subset of voxels, with each voxel denoted as s_k, in the search space, η. In the implementation of the proposed algorithm, a uniform distribution was applied. Using this uniform distribution, voxels in the search space are selected with equal probability.

Once a voxel is selected, an acceptance probability, $\alpha(s_k|s_0)$ (Equation 3.10), is calculated by comparing the neighbours of each selected voxel, s_k, and the voxel of interest, s_0. This acceptance probability is used to determine if each s_k is a realization of $p(\log(f)|\log(v))$. The probability is calculated as the product of Gaussian error statistics for each j^{th} site, denoted $h_k[j]$ and $h_0[j]$, in the neighbourhood of the voxels, s_k and s_0, since neighbouring voxels are assumed to be independent.

$$\alpha(s_k|s_0) = \frac{\prod_j \frac{1}{2\pi\sigma} exp[\frac{-(log(h_k[j]/h_0[j]))^2}{(2\sigma^2)}]}{\prod_j (exp(\lambda))}. \tag{3.10}$$

The λ found in Equation 3.10 is a normalization term that allows $\alpha(s_k|s_0)$ to equal 1 if s_k's neighbours are identical to those of s_0. The term σ controls the shape of the exponential and is based on the variance of the uncorrected image in the log domain. $\alpha(s_k|s_0)$ returns the probability that the voxel s_k is accepted into the set Ω and used to estimate the posterior distribution $p(\log(f)|\log(v))$. Moreover, $\alpha(s_k|s_0)$ is the associated importance weight for the accepted voxel. To determine whether a voxel, s_k, is accepted, a random value, u, is drawn from a uniform distribution. If $u \leq \alpha(s_k|s_0)$, then s_k is accepted into the set Ω or if otherwise, s_k is discarded. This process of selection and acceptance is repeated until a desired number of samples, κ, have been selected from the search space. The posterior distribution is then calculated as a weighted-histogram (Equation 3.11). :

$$\hat{p}(\log(f)|\log(v)) = \frac{\sum_{k=0}^{\kappa} \alpha(s_k|s_0)\delta(log(b(s_k)) - log(v(s_k)))}{Z} \tag{3.11}$$

where $\delta()$ is the Dirac delta function and Z is a normalization term such that

$\sum_{\log(f)} \hat{p}(\log(f)|\log(v)) = 1$. Equation 3.9 can then be calculated with the estimated posterior distribution to find an estimate of the bias field.

3.3 Bias field image correction

Once the bias field estimate $\hat{f}$ is found, the inverse relationship in Equation 3.2 is used to construct the bias field-free image. The bias-free estimate $\hat{w}(s)$ can be denoted as follows:

$$\hat{w}(s) = \frac{v(s)}{\hat{f}(s)}. \tag{3.12}$$

A summary of the MCBC algorithm can be found in Section 3.4.

3.4 Summary of the MCBC algorithm

1. Randomly draw s_k using $Q(s_k|s_0)$ from η
2. Calculate $\alpha(s_k|s_0)$ (Equation 3.10) for each s_k in the subset of randomly drawn voxels from step 1.
3. Draw a random value, u, from a uniform distribution
   if $u <= \alpha(s_k|s_0)$ **then**
   s_k is considered a realization of $p(log(f)|log(v))$ and is accepted to the set Ω
   else
   s_k is not considered a realization of $p(log(f)|log(v))$ and is discarded
   end if
4. Calculate $\hat{p}(log(f)|log(v))$ as a weighted-histogram using Equation 3.11
5. Use $\hat{p}(log(b)|log(v))$ to calculate $\hat{f}$ using Equation 3.9
6. Calculate $\hat{w}(s)$ using the inverse relationship in Equation 3.12 with $\hat{f}(s)$

3.5 Intensity bias correction experimental setup

The proposed MCBC algorithm is compared against five state-of-the-art approaches for performance evaluation:

1. bias-corrected fuzzy C-means (BCFCM) [64]
2. spatial gradient distribution method (SGD) [65]
3. a level-set method (LS) [66]
4. low entropy minimization with a bicubic spline model (LEMS) [67] method
5. surface coil intensity correction (SCIC) [37]

The implementations of LS, SGD and LEMS used for this thesis were provided by the original authors of the respective methods, while the implementation of BCFCM used was provided by a third party [68]. SCIC is used as a baseline for comparison and consistent with [37]. For LEMS, a fourth-order polynomial was used to initialize the bias field and a consistent threshold level across all images was used.

The bias fields and the corresponding corrected endorectal DWI images were generated using MATLAB and the ProCanVAS (Prostate CANcer Visual Analysis System) platform developed at the University of Waterloo Vision and Image Processing (VIP) Research lab. All images were reviewed by a single radiologist with 16 years of experience interpreting body MRI and 11 years of experience interpreting prostate MRI. The uncorrected (UC) and corrected images were reviewed. The proposed approach is intended for volumetric data, however, for the purpose of this thesis, single slices were used for demonstration.

The approaches were evaluated using a combination of physical and synthetic phantoms as well as real patient data. Quantitative analysis is completed using metrics including correlation coefficient, coefficient of variation, Fisher criterion and probability of error. Visual analysis is also completed with specific analysis of computed high b-value DWI and computation time. Three experimental setups were used to compare the proposed MCBC algorithm against other state-of-the-art algorithms for intensity bias correction. In this section the types of data and equipment used are described in more detail.

3.5.1 Synthetic phantom experiment

In the synthetic phantom experiment, a known intensity bias field was added to a non-endorectal coil DWI image to create a synthetic phantom. The bias field was simulated using a Gaussian distribution to imitate the radial nature of the intensity deterioration away from the rectum, where the coil is located. Within the rectum, a circle with zero intensity was added to replicate the lack of signal at the ERC center. A non-endorectal DWI image was used as reference for the synthetic phantom tests due to their lack of bias field effects. The original non-endorectal DWI image and the synthetic phantom are shown in Figure 3.1. This synthetic phantom was evaluated using the correlation coefficient metric and the results are discussed in Section 3.6.1.

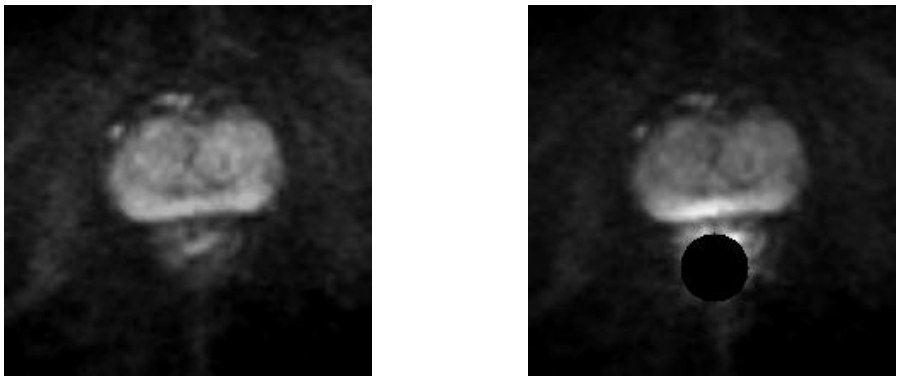

(a) Non-endorectal DWI **(b)** Synthetic Phantom

Figure 3.1. The original non-endorectal DWI (left) used to create the synthetic phantom (right).

3.5.2 Physical phantom experiment

For the physical phantom experiment, images of a multi-modality prostate training phantom from Computerized Imaging Reference Systems Inc (CIRCS Model 053) were used retrospectively. The phantom is contained within a $12 \times 7.0 \times 9.5$ cm clear container made of acrylic. The container has two openings for the probe of 3.2 cm diameter (front) and 2.6 cm diameter (rear). Located inside the container is the prostate replica composed of high scattering Blue Zerdine ($5.0 \times 4.5 \times 4.0$ cm) that is placed in a water-like background gel with little backscatter attenuation ($\leq$ 0.07 dB/cm-MHz). Within the prostate itself, there are three $0.5 - 1.0$ cm lesions placed hypoechoic to the prostate. The urethra and

rectal wall are made of low scattering Zerdine with diameter of 0.70 cm and dimensions $6.0 \times 11 \times 0.5$ cm respectively.

This phantom was then placed in a tub of water to increase signal amplification and placed between cushions to elevate and stabilize the phantom during acquisition as well as improve the realism of the phantom. The phantom was then imaged with the inflatable Medrad Prostate eCoil MR endorectal coil using DWI. DWI was collected using a 3 T GE Discovery MR750 MRI scanner. A central slice imaged previously using $b = 100$ s/mm^2 is used for experimentation and is shown in Figure 3.2.

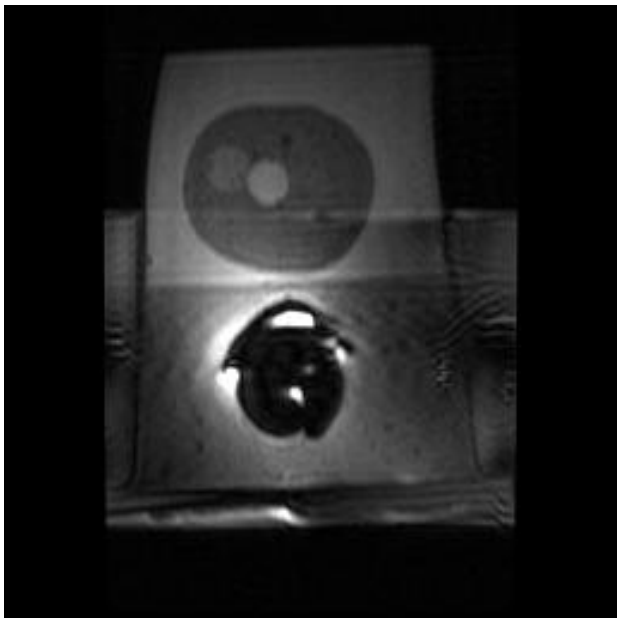

Figure 3.2. The physical phantom imaged using DWI with $b = 100$ s/mm^2 used in the physical phantom experiments.

The display field of view (DFOV) is 14×14 cm with a pixel spacing of 0.55 mm between rows and columns and a slice thickness of 3 mm. The echo time (TE) was 70 ms and repetition time (TR) was $10,000$ ms. This slice was used to evaluate the approaches' correction using coefficient of variation. The results can be found in Section 3.6.2.

3.5.3 Patient experiment

The patient data collected for this experiment obtained approval from the ethics review board of Sunnybrook Health Sciences Centre, Toronto, Canada and was used retrospec-

tively. Informed consent was waived. Seven patient cases were used in this study with acquisitions at $b = 800$ s/mm^2 and $b = 0$ s/mm^2, totaling to 14 cases. Scans were collected using a GE Medical Systems Signa HDxt 1.5 T machine. Imaging parameters for the acquisitions were: two b-values ($b = 800$ s/mm^2 and $b = 0$ s/mm^2), TR ranged from 3400 - 4000 ms, with a median of 4000 ms and TE ranged from 73.8 - 100.608 ms with a median of 74 ms. Slice thickness was 3 mm for all selected slices. The display field of view (DFOV) was 14×14 cm^2. A Hologic endorectal receiver coil was used in all patients with the patients ranging in age from 53-78 years, with a median age of 70 years. All patients underwent MRI as part of clinical indications related to detection or staging of prostate cancer. The patient data was assessed using the Fisher criterion and probability of error with computation of computed high b-value results. The results are presented and discussed in Section 3.6.3.

3.6 Intensity bias correction results

In this section, the intensity bias corrected results of each compared method are measured using quantitative and qualitative techniques to determine whether the proposed MCBC approach is able to improve visualization of the prostate.

3.6.1 Synthetic phantom experiment results

The synthetic phantom was corrected using the various intensity bias correction approaches and evaluated using the correlation coefficient. The correlation coefficient, r, describes how dependent two images are with one another. An $r = \pm 1$ indicates a linear relationship between the two images (they are scalar multiples of one another) while an $r = 0$ indicates that there is no predictability between the two images. The correlation coefficient was calculated for the prostate gland for each corrected image with the original non-endorectal DWI image using the following equation:

$$r = \frac{\sum_i \sum_j (P_{ij} - \bar{P})(Q_{ij} - \bar{Q})}{\sqrt{\left(\sum_i \sum_j (P_{ij} - \bar{P})^2 \right) \left(\sum_i \sum_j (Q_{ij} - \bar{Q})^2 \right)}} \tag{3.13}$$

where i and j describe the dimensions of the images P and Q to be compared and $\bar{P}$ and $\bar{Q}$ indicate their image means.

The correlation coefficients for the bias corrected synthetic phantom are shown in Table 3.1. MCBC exhibits the strongest correlation with the original non-endorectal DWI image within the prostate gland. BCFCM, LS, SGD and SCIC provide some improvement upon the correlation of the uncorrected image by reducing the intensity variation to improve prostate gland visualization. However, these correction approaches still exhibit strong intensity variation in the periperhal zone which leads to lower correlation. LEMS has a high correlation coefficient with the original image as a result of flattening the prostate to remove the intensity bias but at the cost of background artifacts.

Table 3.1. The correlation coefficients for each correction approach compared to the original non-endorectal DWI image. MCBC had the highest correlation with the original DWI (shown bolded). Values are shown in decreasing order.

Method	**Correlation Coefficient**
UC	0.935
MCBC	**0.991**
LEMS	0.985
SCIC	0.981
SGD	0.975
BCFCM	0.961
LS	0.960

3.6.2 Physical phantom experiment results

In the physical phantom experiment, the bias corrected images were used to calculate the coefficient of variation (CV) in a specified region most susceptible to intensity bias (shown in Figure 3.3) to quantitatively assess each approach's bias field removal. A lower CV measure indicates the region of interest has lower variation and since the imaged phantom is homogeneous, this measurement is useful in evaluating the correction's ability to remove the intensity bias. It was calculated using the following equation:

$$\hat{C}_v = \frac{\sigma_r}{\bar{x_r}} \tag{3.14}$$

where $\hat{C}_v$ is the CV value, σ_r is the standard deviation of a region and $\bar{x_r}$ is the mean intensity of a region.

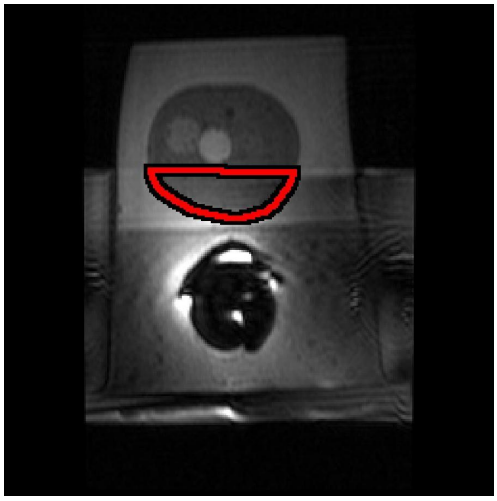

Figure 3.3. The region considered for homogeneity using coefficient of variation (Equation 3.14).

The CVs were calculated for a known homogeneous region in the lower half of the prostate phantom closest to the ERC. CV relates a scalar value to the level of intensity variation in a given area. In an area affected by a bias field, there is increased intensity variation where the strongest intensity appears nearest the ERC and weakens with distance. In this area, the CV value would be high. By removing the intensity variation (the bias field), the CV would be reduced. The images with the lowest CV value are determined to have the least variation in the areas of interest concluding the best bias field removal.

In the next experiment, the bias corrected DWI images of a physical phantom were evaluated for CV and the results are shown in Table 3.2. LEMS showed the lowest CV indicating the least intensity variation within the masked region with MCBC with the next lowest CV. Due to the known homogeneity of the phantom in this area, the CV is a useful indicator that the bias correction by these two approaches is more successful compared to the other methods. Looking more closely at the visual results, it is evident that LEMS' correction is homogeneous in this region, however, nearest the endorectal coil, MCBC reduces the variation more effectively without the presence of background artifacts.

3.6.3 Patient experiment results

For the patient experiments, the Fisher criterion and probability of error were calculated to analyze the separability between the prostate gland and the background following correc-

Table 3.2. Coefficient of variation for each correction approach for the physical phantom. LEMS has the lowest CV with MCBC with the next lowest CV, indicating the lowest variation in the selected homogeneous region (bolded value). Values are shown in increasing order.

Method	Coefficient of Variation
UC	0.237
LEMS	**0.131**
MCBC	0.157
SCIC	0.173
BCFCM	0.205
LS	0.210
SGD	0.240

tion. Increased separability helps to improve the visualization of the prostate for diagnosis and analysis. The aim of this section is to interpret the results.

Fisher criterion

Fisher criterion (FC) analysis was performed on real endorectal DWI bias corrected images to study the separability between the prostate gland and the surrounding background, which is important for segmentation and visualization. It was calculated using the following formula:

$$J = \frac{|\bar{\varpi} - \bar{\varrho}|^2}{\sigma_b^2 + \sigma_p^2} \tag{3.15}$$

where J is the FC value, $\bar{\varpi}$ and $\bar{\varrho}$ are the class means for the surrounding background and the prostate gland, respectively, and σ_b^2 and σ_p^2 are the class variances for the surrounding background and the prostate gland, respectively. The greater the FC value, the greater the delineation between the prostate and the background. This value was also calculated based on the uncorrected image to provide a comparative benchmark and the class means were determined using prostate gland segmentation masks.

The results of the FC analysis are shown in Table 3.3. Considering the FC values of all the methods, MCBC proves to be the most robust at increasing the class separation of the uncorrected image. Improved class separation improves visualization and eases

the process of diagnosis. This method improved upon the FC of the uncorrected image drastically. MCBC's higher FC values show that this approach was able to improve upon the uncorrected image's separation between the prostate and background. BCFCM, LS and SGD showed similar results where there was some improvement with respects to separation but less significant as MCBC. SCIC on the other hand, in most cases, failed to improve the FC of the uncorrected image and instead diminished it. Visual results support these conclusions as the approach is dependent upon a fixed threshold value. The threshold value is used to develop a mask where correction is applied and does not support the accurate estimation of ERC caused bias fields. As a result, SCIC overcompensates for intensity bias in the background. Consequently, the separability of the prostate and the background is impacted and the FC value is diminished. LEMS showed a wide range of FC values, where in some cases, it demonstrated improved separation over the uncorrected image while in others it made the separation worse. This is due to the user-thresholded mask that is applied to the image in order to narrow the range of the bias field. A consistent threshold was used for all cases in order to give fair comparison against the other approaches. A fourth-order polynomial was also used to initialize the bias field. As a result, if the mask is not a reasonable fit to the bias field, LEMS can instead introduce artifacts that decrease the separation of the prostate and the background.

Probability of error

In measuring the separability of the prostate in real endorectal DWI from the background, the probability of error was also calculated. Due to the variability between bias field affected images, a two-class Bayesian classifier was learned using each individual case, where the two classes include the prostate and the background. The individual classes (prostate – P($\rho|u$) and background – P($\beta|u$)) were modeled as normal distributions and learned using maximum likelihood (ML) estimation. The probability of error was calculated as follows:

$$P(\epsilon) = \int min[P(\rho|u), P(\beta|u)]p(u)du \tag{3.16}$$

where ρ and β are the prostate and background classes. A high probability of error indicates that there is a large overlap between the two class distributions and as a result the ML threshold estimate leads to incorrect classifications between the two classes. A lower probability of error indicates that there is better separation between the two classes and fewer voxels are misclassified.

Table 3.3. FC results: MCBC results in the strong separation of the prostate and the background with the highest FC values. Bolded values are the highest values for the particular case.

Case	UC	MCBC	BCFCM	LS	SGD	LEMS	SCIC
1	1.016	2.386	1.271	1.104	1.268	**3.194**	0.245
2	0.779	**1.926**	0.995	1.018	1.280	0.239	0.601
3	0.958	**2.419**	1.221	1.205	1.234	1.395	0.468
4	1.266	**3.543**	1.620	1.556	1.787	0.649	1.141
5	0.976	**2.640**	1.284	1.249	0.938	0.108	0.532
6	1.029	**2.050**	1.289	1.287	1.308	0.293	0.916
7	1.200	**3.312**	1.557	1.255	1.309	2.559	0.720
8	1.309	**4.070**	1.712	1.426	1.612	0.726	1.191
9	0.971	**2.325**	1.246	1.200	0.865	1.070	0.521
10	0.848	**1.727**	1.072	1.060	1.149	0.350	0.629
11	0.883	**2.151**	1.110	0.930	0.930	0.130	0.517
12	0.987	**2.703**	1.267	1.145	1.223	0.386	0.918
13	0.735	1.459	0.907	0.900	**1.174**	0.113	0.106
14	0.738	**1.576**	0.898	0.932	1.098	0.213	0.343
Avg.	0.978	**2.449**	1.246	1.162	1.227	0.816	0.632

Supporting the FC results, the probability of error (Table 3.4) showed that MCBC had the lowest average probabilities of error compared to the other approaches. This demonstrates that MCBC's ML estimation to classify the two classes allows the best separation between the classes with fewest voxels misclassified. Improved separation of the prostate from the background helps to improve visualization of the prostate for diagnosis. BCFCM, LS and SGD showed similar probabilities of error to one another which were also similar to the uncorrected images. This indicates that the separation between the classes was not improved based on the learned ML estimates. LEMS and SCIC had the highest probability of error demonstrating there were many misclassified voxels due to the poor separation of the prostate and background.

Table 3.4. Probability of error results: MCBC demonstrates the lowest average probability of error for all cases indicating it has the lowest chance of misclassifying a voxel incorrectly as compared to the uncorrected image. Bolded values indicate the lowest values.

Case	**UC**	**MCBC**	**BCFCM**	**LS**	**SGD**	**LEMS**	**SCIC**
1	0.335	0.260	0.328	0.349	0.277	**0.198**	0.648
2	0.450	**0.281**	0.410	0.406	0.364	0.552	0.539
3	0.329	**0.250**	0.322	0.318	0.297	0.305	0.674
4	0.189	**0.130**	0.185	0.186	0.196	0.418	0.312
5	0.296	**0.234**	0.298	0.291	0.304	0.722	0.619
6	0.366	**0.270**	0.341	0.333	0.338	0.495	0.435
9	0.242	**0.186**	0.246	0.267	0.243	0.228	0.534
10	0.218	**0.136**	0.215	0.227	0.199	0.471	0.285
11	0.302	**0.264**	0.306	0.305	0.341	0.356	0.625
12	0.340	**0.282**	0.329	0.322	0.312	0.529	0.487
13	**0.260**	0.274	0.278	0.291	0.270	0.717	0.574
14	0.282	**0.214**	0.280	0.280	0.299	0.522	0.349
18	**0.372**	0.381	0.386	0.377	0.428	0.756	0.702
20	0.451	**0.320**	0.419	0.409	0.406	0.555	0.644
Avg.	0.317	**0.249**	0.310	0.311	0.305	0.488	0.531

Computed high b-value DWI results

In this experiment, the intensity bias correction approaches are evaluated for their identification of tumor candidates when used to generate computed high b-value DWI is considered. High b-value DWI, even with the use of an ERC has relatively low SNR. To overcome this problem, a newly-described technique called computed DWI was introduced where DWI images at high b-values are computed using DWI acquisitions at lower b-values. This technique was found to be useful for improved cancer delineation while maintaining image quality [16]. In this experiment, computed high b-value DWI images at $b = 1500$ s/mm^2 generated by the tested methods for a patient case with known prostate cancer and a patient case without prostate cancer are compared to determine which method provides the best tumor visualization following bias correction. The high b-value DWI image is computed using the following formula:

$$S_b = S_0 exp(-b \cdot ADC) \tag{3.17}$$

where S_b is the computed DWI with b-value of b, and ADC refers to the apparent diffusion coefficient. The resulting high b-value DWI images are useful in indicating tumor regions where high cellular density results in low diffusion and high intensity.

The computed high b-value DWI images were evaluated using FC and probability of error as described in Section 3.6.3 to determine the separability of the tumor from the prostate. High b-value computations were calculated for two cases (shown in Figure 3.4 and 3.5). Figure 3.4 shows an example where the high intensity region identifies an area with low diffusion, potentially indicating the presence of a tumor. Due to the bias field created by the ERC (indicated by the blue pointer), it is difficult to delineate the tumor region (indicated with the red arrow). BCFCM, LS, SGD and SCIC are unable to completely remove the bias impacting the peripheral zone (PZ) and this is evident by the bright PZ. The failure to remove this intensity bias near the coil leads to uncertainty whether this region is a tumor candidate or a result of intensity variation. In contrast, LEMS is more successful in delineating the lower region of the tumor, however, the introduction of artifacts near the top of the prostate gland also leads to uncertainty. The artifacts show up as bright regions which could demonstrate the potential for a cancerous region which can be misleading and potentially harmful to diagnosis. MCBC displays the best tumor delineation with the best bias removal displaying the tumor region with high intensity as expected.

In Figure 3.5, an example of non-cancerous tissue is shown where no bright regions are to be expected. The bias field and poor bias correction, however, show as bright

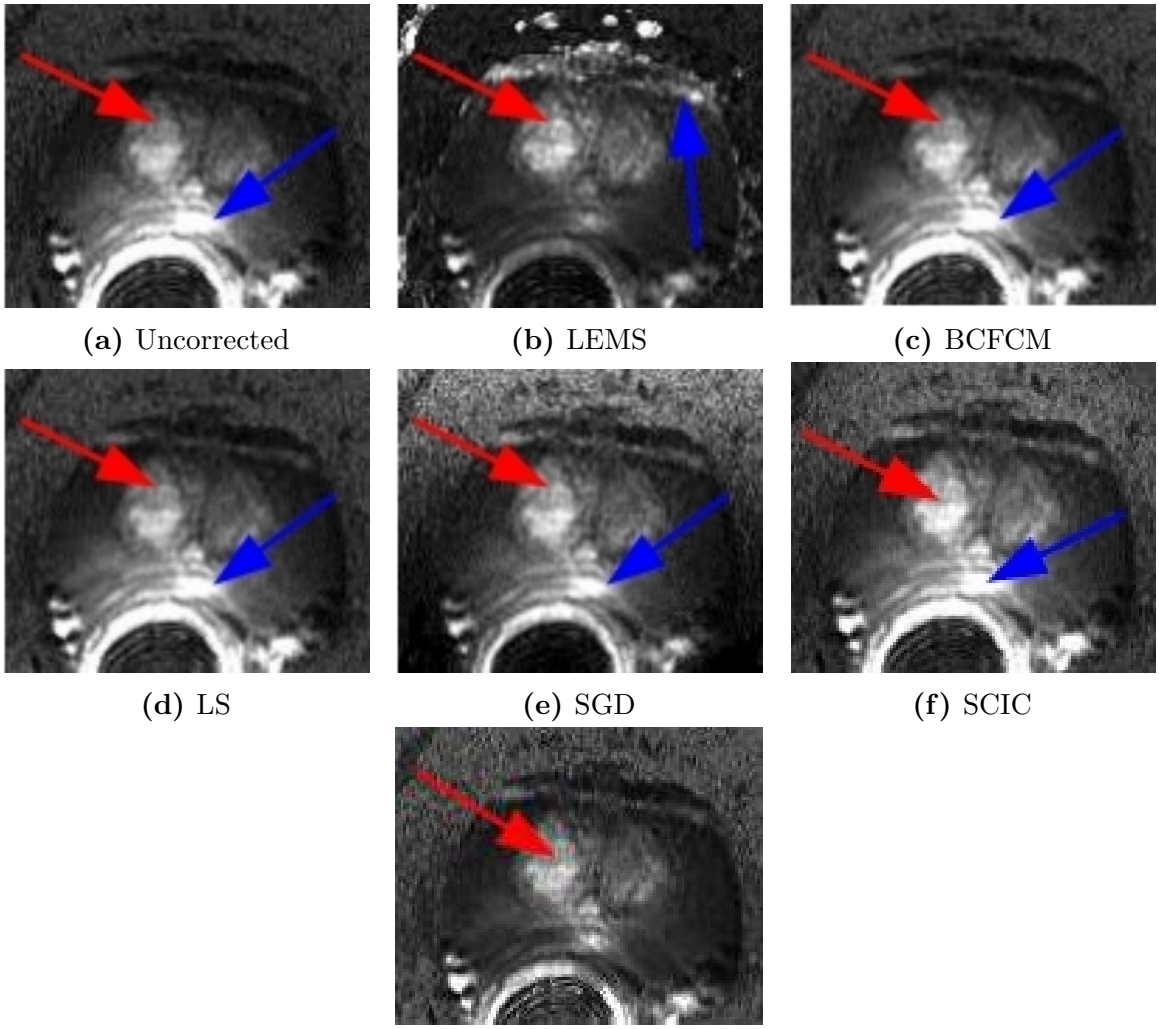

(a) Uncorrected **(b)** LEMS **(c)** BCFCM

(d) LS **(e)** SGD **(f)** SCIC

(g) MCBC

Figure 3.4. High b-value $b = 1500$ s/mm^2 with tumor: The bright intensity of the tumor (red arrow) is most visible in MCBC due to the lack of inhomogeneity (blue arrow) that is apparent in the other approaches.

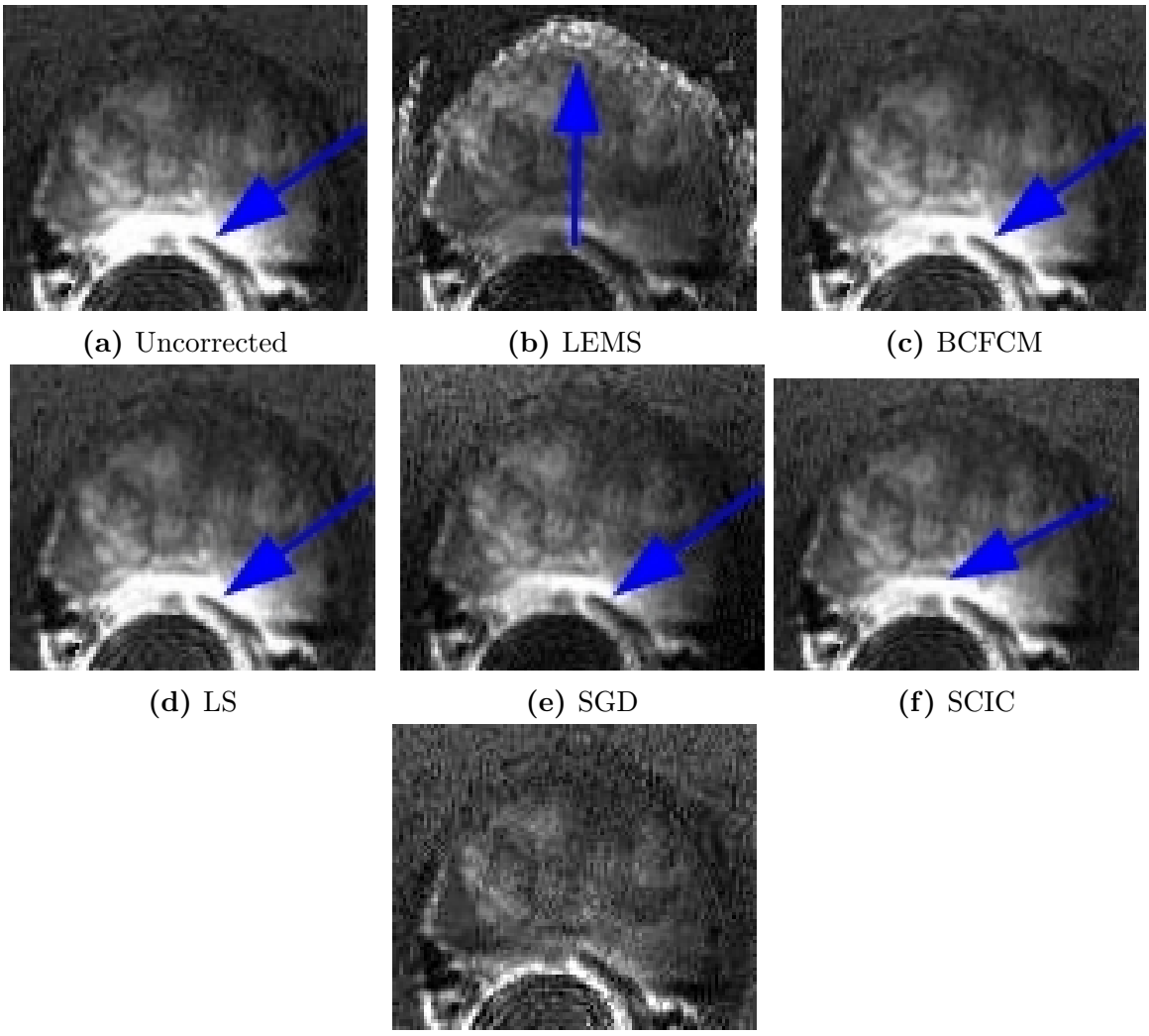

(a) Uncorrected **(b)** LEMS **(c)** BCFCM

(d) LS **(e)** SGD **(f)** SCIC

(g) MCBC

Figure 3.5. High b-value $b = 1500$ s/mm^2 without tumor: The prostate gland appears most even in MCBC while the other approaches exhibit bright intensity regions that are characteristic of tumor regions that are in fact non-existant.

regions in the PZ which make this assumption challenging. BCFCM, LS and SCIC are unable to remove the inhomogeneity while SGD is able to remove some of the bias. LEMS removes all of the inhomogeneity successfully, however, distorts the upper prostate gland by creating the appearance that it is larger than it really is. Due to its strong dependence upon threshold masking for correction, the computed high b-value is not useful due to this inaccurate representation. MCBC shows the best bias correction without distorting the prostate gland, thereby allowing for better visualization.

To quantify the separation of the tumor found in Figure 3.4 from the prostate gland, the FC and probability of error were calculated. The results are shown in Table 3.5. MCBC had the best separation indicated by the high FC value and the lowest probability of error in classifying the tumor from the prostate. Due to its removal of the bias field, MCBC maintains a strong delineation of the tumor from the prostate which is useful in tumor localization and visualization.

Table 3.5. FC and probability of error results for computed high b-value: MCBC shows the highest FC and lowest probability of error supporting the removal of the bias field for strong delineation of the tumor.

Method	Fisher Criterion	Probability of Error
UC	1.019	0.469
MCBC	**3.312**	**0.195**
BCFCM	1.442	0.394
LS	1.425	0.395
SGD	2.952	0.222
LEMS	3.005	0.215
SCIC	2.123	0.302

3.6.4 Visual assessment

Figures 3.8, 3.9 and 3.10 show example slices from three out of the fourteen cases that have been corrected with the discussed methods. In comparison to the other images, the results produced by MCBC visually validate the previous FC and probability of error analyses. In these images, the strong bias field near the ERC has been muted to allow for improved prostate and background delineation aiding in visual analysis. The bias field is still visible in the BCFCM, LS, SGD and SCIC corrected images around the ERC and shows a weak separation between the prostate and the background. SCIC uses a fixed threshold mask to

develop a bias estimate. As such, this mask can lead to poor bias estimation and correction leading to remnants of the intensity bias and weak separability of the prostate from the background.

Similarly, LEMS shows some variation in the PZ region but less than BCFCM, LS, SGD and SCIC, however, the presence of additional artifacts can increase the size of the prostate. This is dependent upon the mask that is initialized using a threshold approach to focus the algorithm upon the prostate. Using a consistent threshold across all images for fair comparison against the other approaches, it is evident that in situations where the mask is a reasonable fit, the results are more favorable. For example, in Figure 3.8 and 3.9, a suitable mask was applied and LEMS is able to compensate for the bias field appropriately (although introducing artifacts in the background). In Figure 3.10, a poor mask is found due to the stronger bias field and as a result the correction is applied on areas not including the prostate, increasing the illumination in the background, thereby reducing the prostate and background separability. Moreover, LEMS appears to remove detail and flatten the prostate gland, making the prostate gland difficult to characterize.

MCBC on the other hand is not subject to a mask and is able to improve separability and illumination variation in the presence of strong and weak bias fields accordingly. With these preliminary results, MCBC shows strong promise in being a useful tool for bias field removal to improve endorectal DWI images for use as diagnostic tools and acting as a pre-processing tool for segmentation.

3.6.5 Timing analysis

The performance of each approach was considered and compared using MATLAB and C++. Tests were completed on a 3.10 GHz AMD Athlon(tm) II X3 445 processor with 4.00 GB of RAM. The MCBC implementation was not optimized for timing performance and author provided implementations were used for the compared approaches. The results are shown below in Table 3.6. BCFCM showed the fastest computation times with performance of 0.094 seconds while LEMS had the slowest average computation time of 119.245 seconds. MCBC shows a middle range performance with an average computation time of 6.359 seconds. SCIC is not included in the timing analysis since the correction is built into the scanners in which case the time to compare against is 0 seconds.

Table 3.6. Computation times: BCFCM has the shortest average computation time with 0.094s while LEMS has the longest average computation time with 119.245s. MCBC shows a middle range performance with 6.359s. All times are shown in seconds and bolded values indicate shortest computation times.

Case	**MCBC**	**BCFCM**	**LS**	**SGD**	**LEMS**
1	6.078	**0.085**	20.773	0.100	76.028
2	6.048	**0.074**	18.903	0.115	84.616
3	6.048	**0.072**	21.669	0.086	77.745
4	6.953	**0.128**	24.189	0.102	90.289
5	6.233	**0.084**	23.803	0.115	255.851
6	6.451	**0.125**	23.366	0.115	92.434
7	6.379	**0.088**	23.805	0.126	78.747
8	6.258	**0.082**	23.389	0.080	85.499
9	6.182	**0.088**	23.706	0.097	76.716
10	6.206	**0.118**	23.585	0.092	83.808
11	6.511	**0.092**	23.717	0.108	237.648
12	6.792	**0.093**	23.284	0.097	88.130
13	6.143	**0.088**	23.452	0.105	255.804
14	6.748	**0.098**	23.332	0.097	86.118
Avg.	6.359	**0.094**	22.927	0.103	119.245

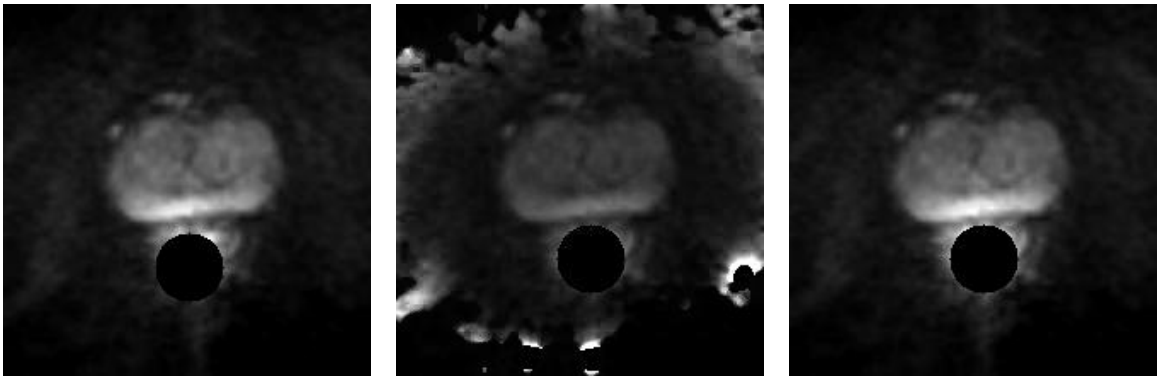

(a) Uncorrected **(b)** LEMS **(c)** BCFCM

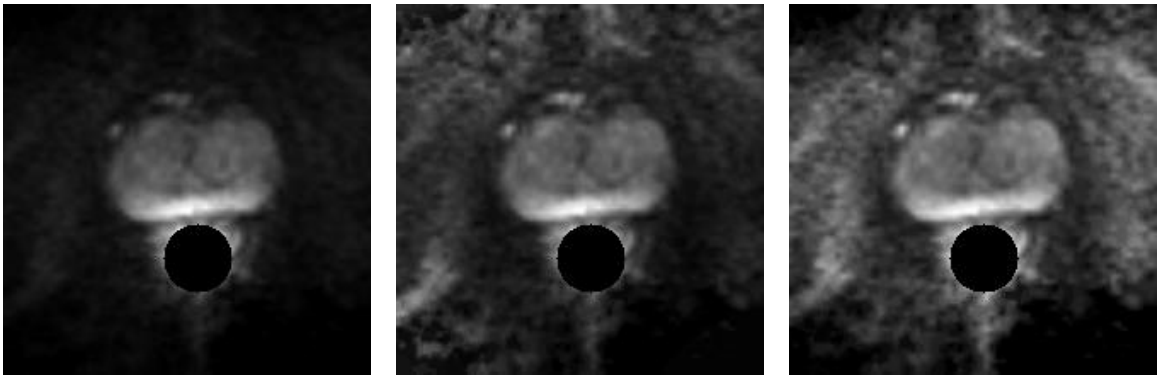

(d) LS **(e)** SGD **(f)** SCIC

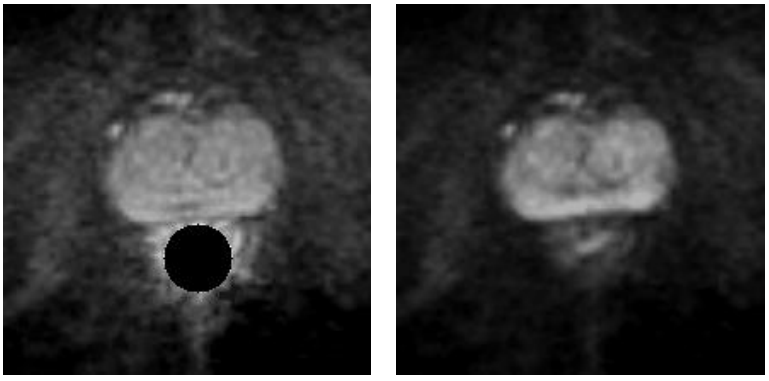

(g) MCBC **(h)** Non-endorectal DWI

Figure 3.6. The bias corrected synthetic DWI phantoms are shown. MCBC displays the best suppression of the intensity bias while the other approaches still display signs of intensity inhomogeneity.

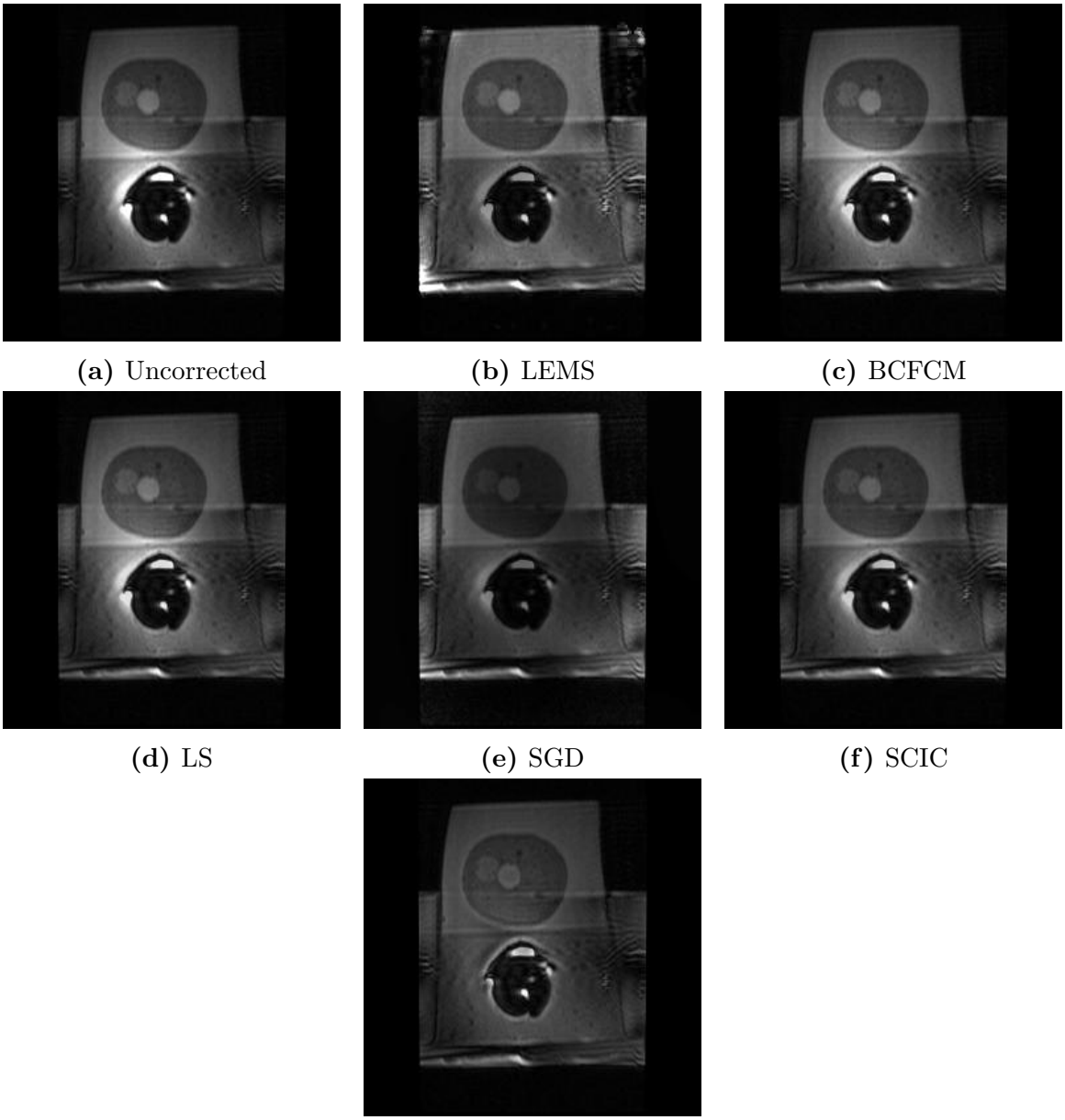

(a) Uncorrected **(b)** LEMS **(c)** BCFCM

(d) LS **(e)** SGD **(f)** SCIC

(g) MCBC

Figure 3.7. The bias corrected DWI phantoms are shown.

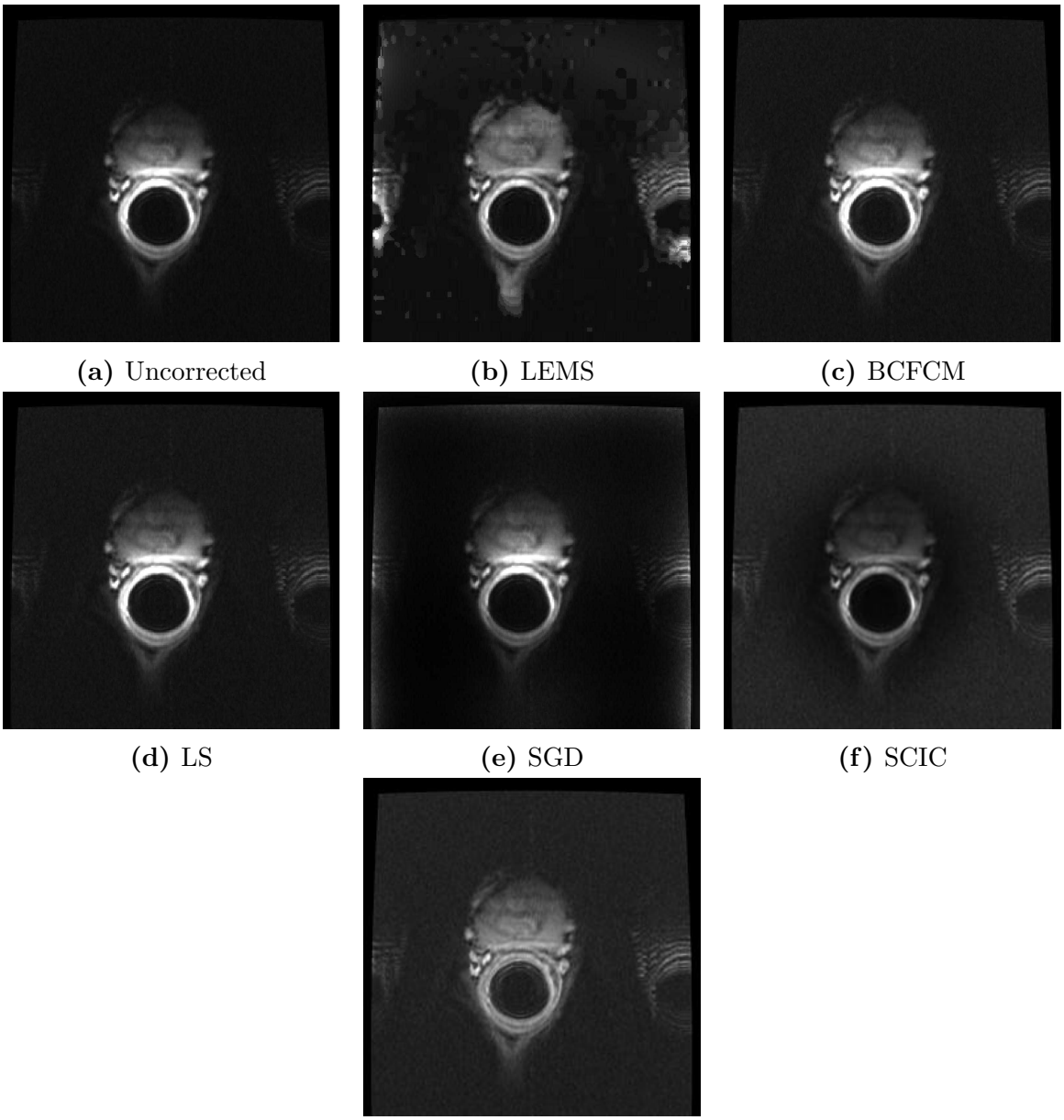

(a) Uncorrected **(b)** LEMS **(c)** BCFCM

(d) LS **(e)** SGD **(f)** SCIC

(g) MCBC

Figure 3.8. Case 1 $b = 800$ s/mm^2: MCBC and LEMS effectively remove the strong bias field found near the ERC which the other methods are unable to compensate for. LEMS, however, exhibits background artifacts and there is still a visible variation that carries from the PZ upwards through the PG in BCFCM, SGD, LS and SCIC.

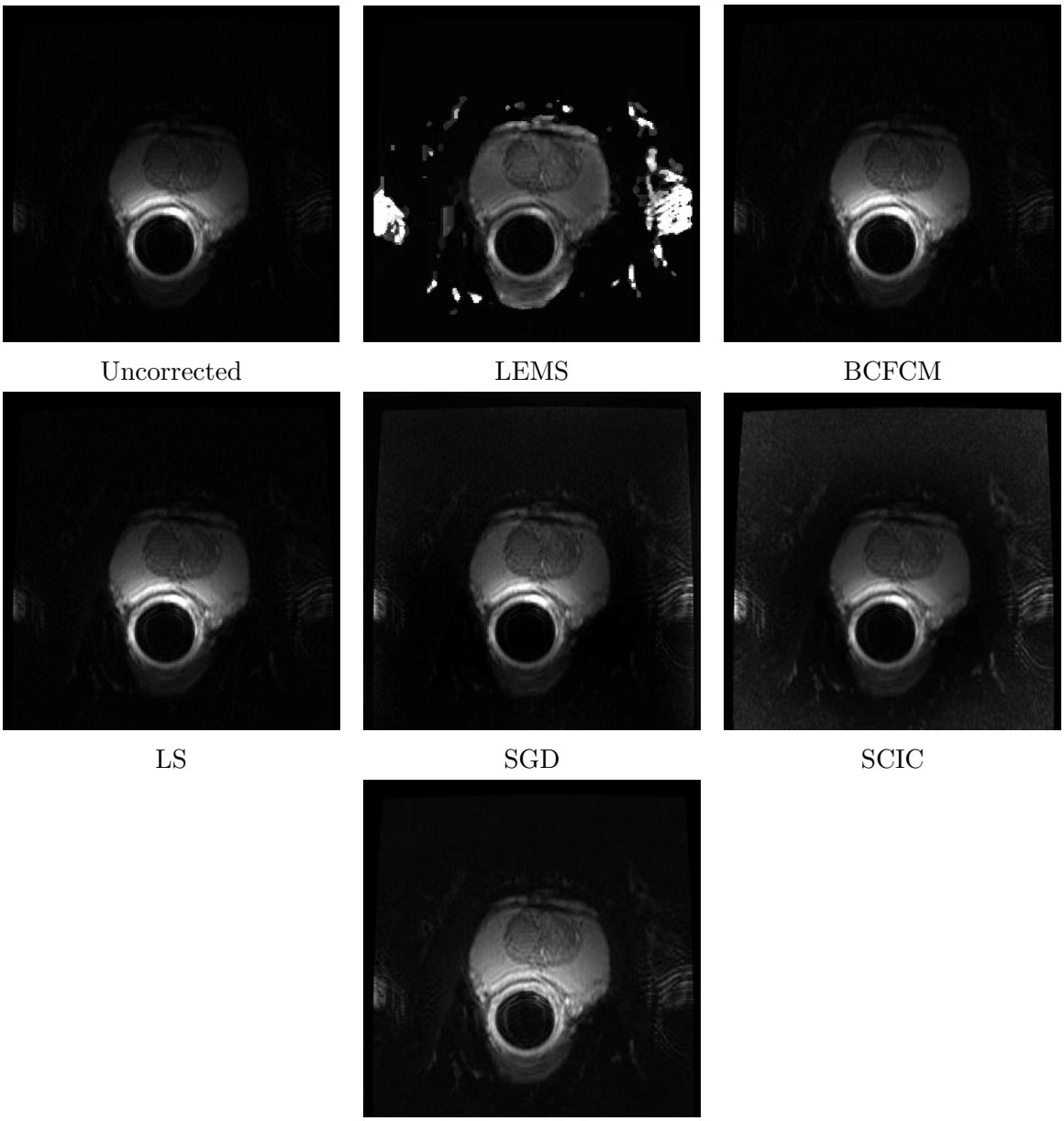

Figure 3.9. Case 4 $b = 0$ s/mm^2: MCBC removes the bias field in the PZ and brightens the PG for better delineation from the background. The bias field can still be seen in BCFCM, LS, SGD and SCIC. LEMS shows additional background artifacts.

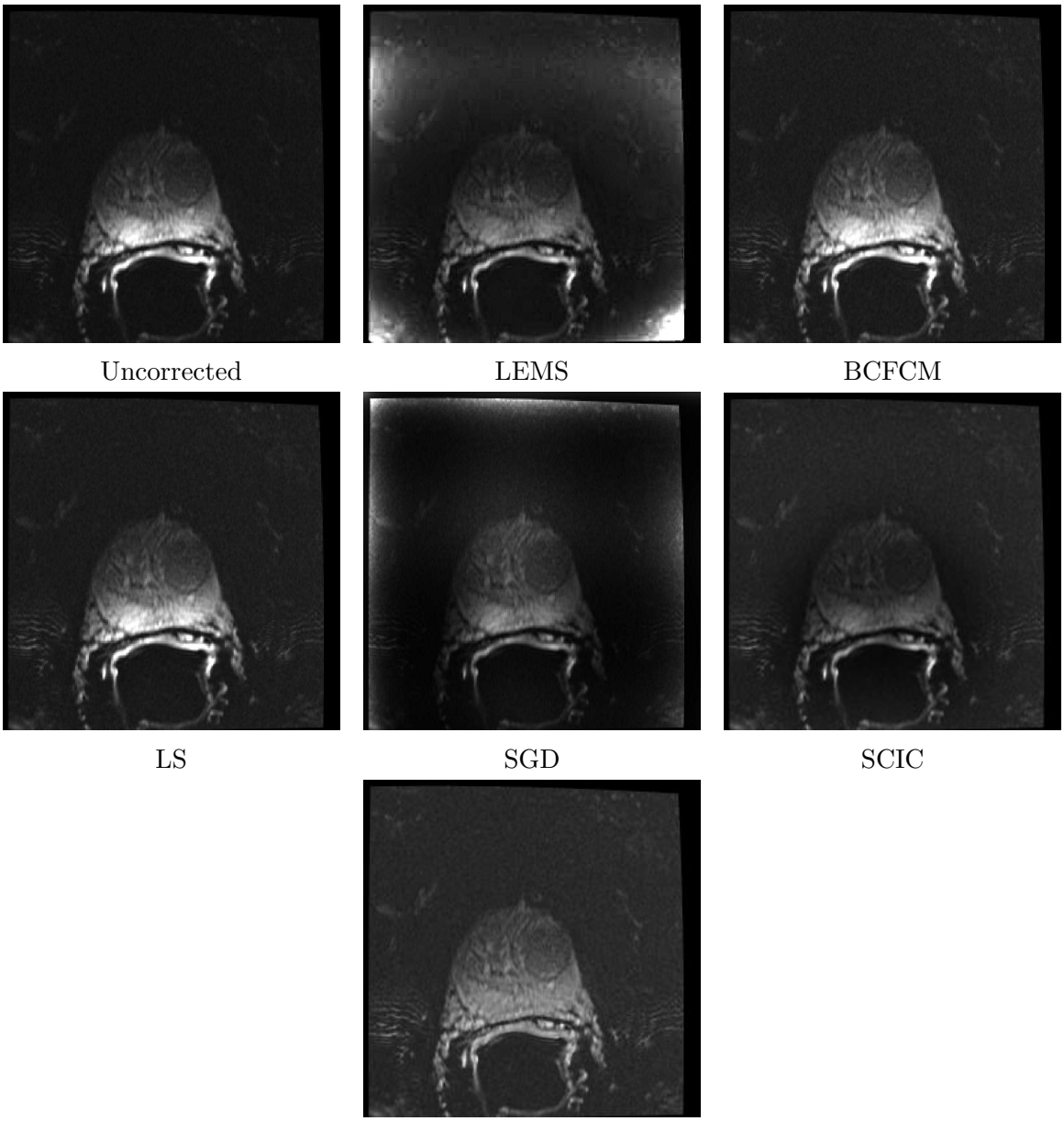

Figure 3.10. Case 13 $b = 800$ s/mm^2: MCBC effectively reduces the bias field across the PZ and PG, resulting in a more consistent intensity across the entire prostate.

3.7 Chapter summary

In this chapter, the Monte Carlo bias correction (MCBC) algorithm for intensity bias field correction in endorectal multi-parametric MRI was introduced. This approach uses a Monte Carlo sampling method to develop a non-parametric estimate of the bias field to be removed for improved image diagnostic capabilities. The resulting bias field estimate from the MCBC approach found in this study appears to result in a better estimate than the compared methods.

Applying a synthetic bias field to a non-endorectal DWI image, MCBC showed high correlation with the non-endorectal DWI image. Then, the resulting corrected MCBC for a physical phantom showed the second least variation within the selected region. In both cases, BCFCM, LS, SGD and SCIC showed minimal improvement upon the inhomogeneity and correlation, failing to remove the strong bias in the PZ nearest the coil. LEMS showed improved bias correction over these other approaches, however, was dependent upon the threshold mask generated and was subject to background artifacts. Moreover, LEMS reduces the detail in the prostate gland and flattens the region making it difficult to distinguish prostate from background. MCBC, however, effectively subdues the intensity inhomogeneity to improve the separability of the prostate from the background with the highest Fisher criterion and lowest probability of error.

High b-value computations of a known tumor case and a no-tumor case were also considered. The purpose of this experiment was to assess bias correction on the improvement of visualization to provide a means of computer-aided clinical decision support for PCa. MCBC's computations showed visually and quantitatively easier visualization of tumors and separation from the prostate while some of the other approaches displayed incorrect indicators of tumor candidates. LEMS even introduced bright background artifacts that made the prostate difficult to delineate and would typically indicate tumor candidates.

Although the intensity bias has been corrected by means of the MCBC approach, the non-stationary noise process in Equation 3.2 still exists. Noise impacts the visualization of the prostate and as a result requires addressing. In the next chapter, a novel algorithm is presented for endorectal multi-parametric MRI for this purpose.

Chapter 4

Noise Compensation in Intensity Bias Corrected Endorectal Multi-parametric MRI

In this chapter, a novel approach for noise compensation on endorectal multi-parametric MRI following intensity bias correction is presented. In Chapter 3, a method for intensity bias correction was presented, however, as shown in Equation 3.2, the noise process becomes spatially variant as a result of the bias correction. To address this issue, the second step of the Monte Carlo framework called adaptive coil enhancement reconstruction (ACER) considers the strategies outlined in Chapter 2 for noise compensation in bias-corrected MRI. ACER uses a spatially-adaptive Monte Carlo sampling approach to estimate the noise-compensated reconstruction while considering the Rician distribution of the underlying data. Furthermore, taking advantage of the ERC's SNR profile, the approach can be adapted for improved performance for a given ERC model. In this chapter, the problem formulation, methodology and implementation is delineated with phantom and patient data results interpreted using quantitative and qualitative analysis techniques.

4.1 Problem formulation

Given the intensity bias-corrected MRI estimate, $\hat{w}$ in Equation 3.12 in Chapter 3, $\hat{w}$ can be expressed as the following relationship:

$$\hat{w}(s) = g(s) + \frac{n(s)}{\hat{b}_f(s)} \tag{4.1}$$

where s is the voxel location, g is the bias-free, noise-compensated reconstruction and $\frac{n(s)}{\hat{b}_f(s)}$ is the non-stationary noise. Knowing the noise process $\frac{n(s)}{\hat{b}_f(s)}$, Equation 4.1 can be reformulated as an inverse problem where the noise-compensated reconstruction g can be found. Bayesian least-squares estimation [69–71] is used to estimate g that minimizes the expected squared estimation error. This formulation is shown below:

$$\hat{g}(s) = \arg\min_{\hat{g}(s)} E\left((g(s) - \hat{g}(s))^2 | \hat{w}(s)\right) = \arg\min_{\hat{g}(s)} \left(\int (g(s) - \hat{g}(s))^2 p(g(s)|\hat{w}(s)) dg(s) \right). \tag{4.2}$$

Taking the derivative of Equation 4.2 with respect to g:

$$\begin{aligned} &\frac{\partial}{\partial \hat{g}(s)} \int (g(s) - \hat{g}(s))^2 p(g(s)|\hat{w}(s)) dg(s) \\ &= \int -2(g(s) - \hat{g}(s)) p(g(s)|\hat{w}(s)) d(g(s)) \\ &= \int (-2g(s) + 2\hat{g}(s)) p(g(s)|\hat{w}(s)) d(g(s)) \\ &= \int -2g(s) p(g(s)|\hat{w}(s)) d(g(s)) + \int 2\hat{g}(s) p(g(s)|\hat{w}(s)) d(g(s)). \end{aligned} \tag{4.3}$$

Then setting the derivative in Equation 4.3 to zero:

$$\begin{aligned} \int g(s) p(g(s)|\hat{w}(s)) dg(s) &= \int \hat{g}(s) p(g(s)|\hat{w}(s)) dg(s) \\ &= \hat{g}(s) \int p(g(s)|\hat{w}(s)) dg(s) \\ &= \hat{g}(s). \end{aligned} \tag{4.4}$$

Simplifying to:

$$\hat{g}(s) = \underbrace{\int g(s) p(g(s)|\hat{w}(s)) dg(s)}_{E(g(s)|\hat{w}(s))}. \tag{4.5}$$

In Equation 4.5, $\hat{g}(s)$ can be estimated using the conditional mean of $g(s)$ on $\hat{w}(s)$, $E(g(s)|\hat{w}(s))$, or the mean of the posterior distribution, $p(g(s)|\hat{w}(s))$. An estimate of the posterior distribution, $p(g(s)|\hat{w}(s))$, can be calculated using a spatially-adaptive importance-weighted Monte-Carlo sampling approach. The approach is adapted to account for the non-stationary Rician characteristics of MRI magnitude data. This is explained in more detail in the next section.

4.2 Spatially-adaptive Rician distributed Monte Carlo posterior estimation

MRI magnitude data is Rician distributed, following:

$$f(x|\nu,\Phi) = \frac{x}{\Phi^2} exp\left(\frac{-(x^2+\nu^2)}{2\Phi^2}\right) I_0\left(\frac{x\nu}{\Phi^2}\right), \quad x > 0; \nu, \Phi \geq 0, \tag{4.6}$$

where Φ and ν are parameters that control the distribution's scale and skew and I_0 is the modified Bessel function of the first kind with order zero. As a result of coil intensity correction, the data's Rician distribution becomes spatially-dependent and results in the following distribution, where $x > 0; \nu(s), \Phi \geq 0$:

$$f(x|\nu(s),\Phi(s)) = \frac{x}{\Phi(s)^2} exp\left(\frac{-(x^2+\nu(s)^2)}{2\Phi(s)^2}\right) I_0\left(\frac{x\nu(s)}{\Phi(s)^2}\right) \tag{4.7}$$

This distribution can be accounted for in estimating the posterior distribution via an importance-weighted Monte Carlo sampling approach [72]. The approach forms Ω, a set of samples and importance weights selected from a search space, η. Voxels, s_k, are selected in a region around a voxel of interest, s_0, and from these samples, a subset are collected randomly using an instrumental distribution, $Q(s_k|s_0)$, such as a uniform distribution. For each randomly drawn voxel, s_k, an acceptance probability, $\alpha(s_k|s_0)$ (Equation 4.8), is calculated which indicates the probability that the neighbourhood of s_k is similar to the neighborhood of s_0. The acceptance probability is shown below as the product of probabilities at each location, j, given the neighbouring voxels are independent:

$$\alpha(s_k|s_0) = \frac{\prod_j \frac{x}{\hat{\Phi}(s_0)^2} \exp\left(\frac{-(x^2+\hat{\nu}(s_0)^2)}{2\hat{\Phi}(s_0)^2}\right) I_0\left(\frac{x\hat{\nu}(s_0)}{\hat{\Phi}(s_0)^2}\right)}{\prod_j \lambda} \tag{4.8}$$

where $x = h_k[j] - h_0[j]$. The terms $h_k[j]$ and $h_0[j]$ denote the j^{th} voxels in the neighbourhoods around s_k and s_0. The variable λ normalizes $\alpha(s_k|s_0)$ so that in the case the neighbours of s_k are duplicates of s_0, $\alpha(s_k|s_0) = 1$. The variables $\hat{\Phi}(s_0)$ and $\hat{\nu}(s_0)$ are the estimated scale and skew respectively, for the voxel of interest, s_0 (their estimation is explained in more detail in the following section). This acceptance probability is used to determine if the sample s_k is a realization of the posterior $p(G(s)|V(s))$ and should be accepted into the set Ω. The acceptance probability reformulates the Rician-distributed statistics to handle the non-stationarity of the coil-intensity corrected MRI data when deciding whether a voxel is accepted or rejected. To use the acceptance probability, a random value u is first generated from a uniform distribution. Then, the voxel s_k is accepted into the set if $u \leq \alpha(s_k|s_0)$, otherwise it is rejected. The process of selection and acceptance is continued until κ samples are chosen from the search space. The posterior distribution estimate can then be calculated using a weighted-histogram [72]:

$$p(g(s)|\hat{w}(s)) = \frac{\sum_{k=0}^{\kappa} \alpha(s_k|s_0)\delta(g(s) - \hat{w}(s_k))}{Z} \tag{4.9}$$

where $\delta()$ is the Dirac delta function and Z is a normalization term to enforce $\sum_k^{\kappa} p(g_k|\hat{w}_k) = 1$. The posterior distribution can then be used to calculate the noise-compensated reconstruction $\hat{g}(s)$ using Equation 4.5.

4.3 Non-stationary unified ERC parametric model

To estimate the posterior distribution $p(g(s)|\hat{w}(s))$ in a spatially-adaptive manner, the scale and skew parameter of each voxel of interest, $\hat{\Phi}(s_0)$ and $\hat{\nu}(s_0)$, are estimated using maximum likelihood estimation,

$$\hat{\theta}_{ML} = argmax_{\theta} f(x|\theta) \tag{4.10}$$

where x are the observed intensities in $\hat{w}(s)$ and θ are the parameters to be estimated: in this case, the scale parameter, $\hat{\Phi}(s_0)$, and the skew parameter, $\hat{\nu}(s_0)$. To refine the scale estimation, an existing SNR profile, defined as $\gamma(\theta)$, which is characteristic to a given ERC, is fitted. Given an ERC, an SNR profile can be mapped to characterize the change in SNR as a function of distance from the ERC surface. Literature has shown that the ERC SNR profile differs from a rigid and inflatable coil, however share a common trend where there is

an SNR gain nearest the coil surface which diminishes with distance [73–75]. Considering the SNR depth profile from posterior to anterior of a rigid coil, a sharp increase in SNR of 3 to 5 times the normal SNR is demonstrated at the ERC surface. This increase is followed by a decrease through the peripheral zone and central gland. Despite the quick decline in SNR, the peripheral zone still experiences a gain in SNR of 1.5 to 3 times. The continual decrease then finds the central gland with only a fraction of the SNR [73–75]. An inflatable coil has demonstrated a weaker response with less SNR increase near the coil. In addition to the variation between SNR profiles for inflatable and rigid ERC, ERC brands have their own characteristic profiles which can be determined by measuring phantoms. The particular parametric ERC model used in the experiments is discussed in more detail in Section 4.5. The full algorithm, Adaptive Coil Enhancement Reconstruction (ACER), is summarized in Section 4.4.

4.4 Summary of the ACER algorithm

1. Perform model fitting to estimate local scale map, $\hat{\Phi}(s)$, using the ERC's SNR profile $\gamma(\theta)$

2. Using the instrumental distribution, $Q(s_k|s_0)$, select a subset of voxels randomly from the neighbourhood of the voxel of interest s_0 in $\hat{w}$.

3. Calculate the acceptance probability, $\alpha(s_k|s_0)$, for each s_k in the subset of selected voxels in step 2.

4. Select a random value, u, from a uniform distribution
   if $u <= \alpha(s_k|s_0)$ **then**
   The voxel, s_k, is considered a realization of $p(g(s)|\hat{w}(s))$ and is accepted to the set Ω
   else
   The voxel, s_k, is not a realization of $p(g(s)|\hat{w}(s))$ and is discarded
   end if

5. Calculate posterior distribution as weighted histogram using $\alpha(s_k|s_0)$ for all s_k in Ω (Equation 4.9)

6. Use posterior distribution to calculate $\hat{g}(s_0)$ (Equation 4.5)

7. Repeat steps 2 - 6 for each voxel in $\hat{w}(s)$

4.5 Implementation

In this section, the implementation is discussed in more detail, in particular the unified ERC parametric model used and the posterior distribution estimation. Two SNR profiles were modeled using the findings from Venugopal *et al.* [73] for two ERC's: a Hologic rigid ERC and a Medrad inflatable ERC. As discussed previously, each ERC has its own characteristic SNR profile and it can be used for more accurate compensation of MRI noise that is amplified using PURE correction. In this ACER implementation, the phantom data used the Medrad inflatable ERC and as such, the unified ERC parametric model was modeled after the Medrad inflatable ERC SNR profile presented by Venugopal *et al.* [73]. The patient data used was a combination of cases using the Medrad inflatable ERC or the Hologic rigid ERC. The inflatable and rigid ERC SNR profiles demonstrate a 1 and 5-fold improvement in SNR at the ERC surface respectively with an exponential drop leading to a final abrupt drop. The final abrupt drop in SNR is found at 4.6 cm and 4.8 cm from the ERC surface where there is low SNR. Following Venugopal *et al.*'s work as well as experiments, the following model, $\gamma(\theta)$, was found to be effective:

$$\gamma(\hat{\Phi}, \hat{\nu})(s_0) = \begin{cases} max(t_1(s), t_2(s)), & \text{if } s \geq r_{ERC} \\ \psi\hat{\Phi}, & \text{if } s < r_{ERC} \end{cases} \tag{4.11}$$

where

$$t_1(s) = \frac{\omega\hat{\Phi}}{1 + \left(\frac{D(s)}{D_0}\right)^{2\zeta}} - \omega\hat{\Phi}, \qquad t_2(s) = -exp(-\varphi|D(s)|)$$

$$D(s) = \sqrt{(X - x_0)^2 + \rho(Y - y_0)^2}$$

where r_{ERC} corresponds to the ERC radius and ψ is a scalar value which adjusts the estimated scale parameter $\hat{\Phi}$ (Equation 4.10). The function, $f_1(s)$, is a Butterworth model that is scaled by a scalar value β and the estimated scale parameter $\hat{\Phi}$ to accommodate the sharp drop in SNR at the ERC surface. The term, $D(s)$, is an elliptical distance map which approximates the elliptical SNR profile demonstrated by the ERC, which is centered at the ERC's center, (x_0, y_0). The parameter ρ controls the major axis of the ellipse for more fine control to appropriately approximate the ERC SNR profile. The other parameters D_0 and n define the slope and flatness of the Butterworth model respectively. The second function,

$t_2(s)$, is an exponential model that is scaled by φ and models the exponential decline found in the ERC SNR profiles through the peripheral zone and central gland regions. Figure 4.1 shows the cross-section of the ERC variance parametric model from the center of the ERC coil.

4.6 Noise compensation experimental setup

To validate the ACER algorithm's performance, it was analyzed against three other state-of-the-art approaches for noise compensation in MRI:

1. an optimized variance-stabilizing transformation for Rician distributions (ROVST) [28]
2. removal by a multi-resolution adaptive non-local means approach (ANLM) [53]
3. linear minimum mean squared error estimator (LMMSE) [59].

The ROVST, LMMSE and ANLM codes used for comparison were provided by their respective authors. All approaches were implemented using MATLAB and the parameters were selected to provide a reasonable balance between prostate detail and noise compensation in the background. A set of experiments using the physical phantom described in Chapter 3 and real patient data were executed for evaluation. In this section, the experimental setups for both experiments are explained in more detail. The results of the experiments can be found in Section 4.7.

4.6.1 Phantom experiment

The multi-modality prostate training phantom used in the physical phantom experiments for the MCBC algorithm was used again for ACER validation. The specifications can be found in Section 3.5.2. For this experiment, the phantom was imaged using an inflatable Medrad Prostate eCoil MR endorectal coil using T2 MRI and DWI. Both T2 and DWI MRI were acquired with the built-in pre-calibration coil intensity correction approach by GE called Phased array UnifoRmity Enhancement (PURE). PURE applied using one excitation with a 3 T GE Discovery MR750. The three phantom data sets were acquired using:

1. DWI $b = 0$ s/mm^2

2. DWI $b = 1000$ s/mm^2

3. T2 and the central slice selected for experimentation

As a result of PURE correction, the cushion in these slices are emphasized by a noise band shown in red in Figure 4.2 for T2. To focus on the phantom itself, these slices were cropped. The display field of view (DFOV) is 16×16 cm with a voxel spacing of 0.3 mm between rows and columns for DWI acquisitions and 0.6 mm between rows and columns for T2 acquisitions. Both DWI and T2 had common slice thicknesses of 3 mm. The echo time (TE) for T2 was 107 ms while the TE for DWI was 72 ms. The repetition time (TR) for T2 was $3,200$ ms and $10,000$ ms for DWI. Central slices from each modality were then considered for SNR and CNR. The results are discussed in Section 4.7.1.

4.6.2 Patient experiment

The second experiment evaluates the image reconstruction performance of the various tested approaches on endorectal T2 axial MRI with PURE within a clinical scenario. The data was collected and then selected for this study retrospectively using a GE Discovery 1.5 T Signa HDxt MRI scanner, a Medrad eCoil inflatable ERC or a Hologic rigid ERC. Institutional research ethics board approval and patient informed consent for this study was obtained. For the purpose of evaluating imaging reconstruction performance, fourteen patient cases were used in this study. Eleven patients were imaged using an inflatable Medrad coil and the central slices were selected for analysis. Three patients were imaged using a rigid Hologic coil and three slices were selected from each volume and considered as a separate case. The patients ranged in age from $54 - 79$ years with a median age of 72 years. The data was collected using 0.5 excitations (NEX) with echo times ranging from $100 - 107$ ms (median echo time of 104 ms) and repetition times of $3,400$ ms. Each slice has a DFOV of 16×16 cm with a voxel spacing of 0.3 mm between rows and columns and a slice thickness of 3 mm. The central slices from each patient case were assessed using SNR, CNR and edge preservation and 3 cases were selected to be qualitatively assessed via a subjective scoring method. The findings are summarized in Section 4.7.2.

4.7 Noise compensation results

In this section, the results of the phantom and patient experiments are presented and discussed. Each approach's performance is considered carefully using a variety of metrics with discussion of any limitations.

4.7.1 Phantom experiment results

For the phantom experiments, the noise suppression approaches were compared using signal-to-noise ratio (SNR), contrast-to-noise ratio (CNR) and visual analysis. P-values were also calculated to determine the statistical significance of the SNR and CNR results. The null hypothesis used was that a given correction approach had no improvement for a subjective metric as compared to the uncorrected image. P-values were calculated for a two-tailed normal distribution with a statistical significance level of 5%. Details of the experimental setup are included in the Section 4.6.1.

SNR and CNR

Due to the known homogeneity of the phantom, for quantitative analysis, SNR and CNR were calculated for two regions: one region on the phantom farthest away from the coil and a second region on the prostate itself. These regions are shown in Figure 4.3 in the uncorrected image in blue and red respectively. SNR and CNR (in decibels) were calculated as follows:

$$SNR = 20\log\frac{\bar{x}_b}{\sigma_b}, \qquad CNR = 20\log\frac{|\bar{x}_b - \bar{x}_p|}{\sigma_b} \tag{4.12}$$

In the SNR equation, the parameter, $\bar{x_b}$, defines the mean value of the region and σ signifies the standard deviation of the region. In CNR, $\bar{x}_b$ and $\bar{x}_p$, denote the mean values of the selected background and prostate regions respectively and σ_b is the standard deviation of the background region which is more indicative of the noise process.

The final SNR and CNR results are shown in Tables 4.1 and 4.2 with visual results for the T2 phantom case in Figure 4.3. All approaches demonstrated improvement upon the uncorrected (UC) slice with the proposed approach, ACER, having the highest average SNR in the selected background and prostate regions. The uncorrected (UC) slice refers to the slice with no application of any algorithm. ROVST and LMMSE proved to have the next best SNRs in the two regions however, considering the visual results, noise was under or overcompensated with deterioration of structure. In the case of DWI at $b = 1000\ \mathrm{s/mm^2}$, where noise was more prominent and contrast was already low, ROVST had greater SNR metrics over ACER however, at the cost of structure preservation. Finally, ANLM exhibited the least SNR improvement in both selected regions, indicating an inaccurate noise estimate.

Table 4.1. Phantom SNR analysis of a selected background and prostate region (in dB with highest measures in bold). ACER proved to have the greatest SNR improvement in the background and prostate regions. ANLM showed an inaccurate noise variance estimate which led to less significant SNR improvement.

	Background SNR					**Prostate SNR**				
Case	**ACER**	**ROVST**	**LMMSE**	**ANLM**	**UC**	**ACER**	**ROVST**	**LMMSE**	**ANLM**	**UC**
$DWI_{b=0}$	**33.2**	32.0	31.6	30.9	30.6	**27.0**	26.8	26.7	26.2	26.1
$DWI_{b=1000}$	27.5	**27.6**	26.4	26.0	25.9	27.3	**27.5**	26.9	25.9	25.7
T2	**29.2**	27.0	27.6	27.0	26.9	**27.2**	26.7	26.9	26.7	26.7
Avg.	**30.0**	28.9	28.5	27.9	27.8	**27.2**	27.0	26.8	26.3	26.2

Table 4.2. Phantom CNR analysis based on the selected background and prostate regions (in dB with highest measures in bold). ACER demonstrated the greatest improvement in CNR illustrating its capacity to augment the detail within the prostate.

Case	**ACER**	**ROVST**	**LMMSE**	**ANLM**	**UC**
$DWI_{b=0}$	**27.1**	25.9	25.4	24.7	24.5
$DWI_{b=1000}$	**20.9**	21.0	19.7	19.4	19.4
T2	**19.7**	17.6	18.1	17.5	17.5
Avg.	**22.6**	21.5	21.1	20.5	20.4

CNR analysis (Table 4.2) showed that ACER had the highest average CNR. ROVST had the second highest average CNR and ANLM with the least improvement. These results indicate ACER's ability to increase the contrast between the background and prostate regions, thereby improving the visibility of detail within the prostate.

P-values (Table 4.3) were also calculated for the SNR and CNR results to verify the statistical significance of the differences between the average SNR and CNR compared to the uncorrected slices. ACER and LMMSE proved their greater average background SNRs over the uncorrected slices were statistically significant with p-value scores of less than 0.05. ACER additionally demonstrated statistical significance for CNR. The other approaches instead had p-values greater than 0.05 indicating the change over the uncorrected slices was not representative of any notable change. For the prostate SNR, all approaches demonstrated statistically insignificant results with p-values greater than 0.05.

Table 4.3. The p-values for the metrics measured for the phantom experiments. Values below 0.05 are shown bolded which indicate the average score across the cases has statistical significance. ACER and LMMSE approaches are the only approaches to have statistically significant results over the uncorrected slices.

Metric	ACER	ROVST	LMMSE	ANLM
Background SNR	**0.02**	0.16	**0.04**	0.27
Prostate SNR	0.10	0.25	0.14	0.18
CNR	**0.02**	0.16	0.05	0.24

The noise suppressed T2 phantom slices for each approach are shown in Figure 4.3. The proposed method demonstrates the best noise compensation while enhancing the detail contrast within the prostate. LMMSE and ROVST also compensate for noise however at the cost of visible structure and edge blurring.

4.7.2 Patient experiment results

The noise suppression approaches were then compared using patient data by analyzing SNR, CNR (Equation 4.12), edge preservation (Equation 4.13) and subjective scores. P-value analysis was also included to determine the statistical significance of the results. Experimental setup details can be found in Section 4.6.2.

SNR and CNR

For the SNR and CNR assessment, a high noise, structure-free region in the background was selected similar to the phantom experiments. A second homogeneous region with higher intensity was then selected for CNR calculation. The results are shown in Table 4.4 where all approaches improved upon the background SNR of the uncorrected slice. In the case of background SNR, ACER had the highest average SNR with ROVST in second. The visual results for ROVST and LMMSE demonstrated that in regions far away from the ERC, noise was effectively removed however, at the cost of detail within the prostate. ACER and ANLM were more effective in retaining the prostatic detail, with ACER having an average improvement over the uncorrected slice of 11.7 dB. Similar to the background SNR results, ACER had the highest average CNR with ROVST in second. ACER demonstrated an average 11.2 dB improvement over the uncorrected slice in CNR. Subsequent p-value analysis (Table 4.5) showed the average improvement over the uncorrected slices for each approach was statistically significant with p-values of less than 0.05.

Edge Preservation Measurement

The edge preservation (EP) measurement evaluates image edge degradation. The EP measurement compares the noise-free reconstruction with the uncorrected image and can be calculated as follows [76]:

$$\Upsilon = \frac{\Sigma(\bigtriangledown^2 V - \overline{\bigtriangledown^2 V}) \cdot (\bigtriangledown^2 \hat{G} - \overline{\bigtriangledown^2 \hat{G}})}{\sqrt{\Sigma(\bigtriangledown^2 V - \overline{\bigtriangledown^2 V})^2 \cdot \Sigma(\bigtriangledown^2 \hat{G} - \overline{\bigtriangledown^2 \hat{G}})^2}} \tag{4.13}$$

where $\bigtriangledown^2 V$ and $\bigtriangledown^2 \hat{G}$ are the Laplacian of the intensity bias corrected image and noise-free reconstruction respectively using a 3×3 filter. The parameters, $\overline{\bigtriangledown^2 V}$ and $\overline{\bigtriangledown^2 \hat{G}}$, are the mean values of a neighbourhood around $\bigtriangledown^2 V$ and $\bigtriangledown^2 \hat{G}$. An image where there is perfect EP results in a measurement of $\Upsilon = 1$. This refers to the technique's ability to retain the structure and edges of the image. For the purpose of this study, since noise can be recognized as edges or details, the EP metric is calculated for the prostate gland only using a user defined mask. This region was selected for high SNR and high importance for detail preservation.

Considering the EP of the noise compensation approaches (Table 4.6), ANLM had the highest average EP with ACER having the second highest. In the real T2 cases, noise was more prominent than compared to the phantoms and as a result, more compensation was

Table 4.4. The patient experiment CNR of two regions and the SNR of a background region are shown (largest values are shown in bold). ACER demonstrates an average increase of 11.7 dB and 11.2 dB for SNR and CNR respectively over the uncorrected (UC) slice which has no noise suppression applied.

	Background SNR					CNR				
Case	**ACER**	**ROVST**	**LMMSE**	**ANLM**	**UC**	**ACER**	**ROVST**	**LMMSE**	**ANLM**	**UC**
1	**34.2**	22.6	31.5	23.1	19.4	**37.0**	25.3	34.5	25.8	22.1
2	**26.8**	21.7	25.7	21.1	18.5	**31.3**	26.2	30.7	25.7	23.0
3	33.1	**34.7**	32.2	26.6	19.6	36.1	**37.7**	35.3	29.6	22.6
4	32.3	**36.3**	34.8	27.7	20.2	30.6	**34.6**	33.3	26.0	18.4
5	**34.1**	33.4	32.5	26.7	22.1	**29.1**	28.4	27.6	21.7	17.2
6	**34.8**	31.6	33.1	26.5	19.9	**30.9**	27.9	29.5	22.7	16.1
7	**34.1**	33.2	33.3	25.7	22.3	**33.6**	32.7	32.9	25.2	21.8
8	32.6	**36.2**	33.9	27.3	19.5	35.6	**39.2**	37.0	30.3	22.5
9	33.6	**35.0**	34.5	27.4	19.6	34.6	**36.0**	35.7	28.5	20.7
10	34.0	**37.0**	35.7	27.6	19.6	33.0	**36.2**	35.1	26.7	18.8
11	**33.0**	27.9	25.4	21.0	13.8	36.1	**41.0**	39.2	34.0	26.8
12	**26.5**	23.5	20.3	20.1	13.2	**26.8**	23.8	20.7	20.4	13.5
13	28.1	**28.2**	19.0	22.3	13.3	24.8	**24.9**	15.9	19.0	10.0
14	22.8	**24.9**	20.4	21.4	13.7	22.3	**24.5**	20.3	21.1	13.4
15	**25.9**	23.9	18.4	20.7	13.2	**26.6**	24.6	19.4	21.4	13.8
16	25.4	**25.6**	21.5	21.5	14.1	24.7	**24.9**	21.2	20.9	13.5
17	24.8	**25.7**	19.6	21.4	13.4	24.0	**25.0**	19.3	20.7	12.6
18	**19.2**	13.1	16.8	15.0	12.8	**17.9**	11.7	15.5	13.6	11.4
19	**18.7**	13.3	16.0	15.5	12.6	**18.3**	12.8	15.7	15.1	12.2
20	12.9	11.9	**13.8**	13.0	11.7	10.6	9.5	**11.5**	10.6	9.3
Avg.	**28.3**	27.0	25.9	22.6	16.6	**28.2**	27.3	26.5	22.9	17.0

Table 4.5. The p-values for the metrics measured for the patient experiments. Values below 0.05 indicate the average score for all slices corrected by each approach represents statistically significant change from the uncorrected slices. All approaches have p-values below 0.05.

Metric	**ACER**	**ROVST**	**LMMSE**	**ANLM**
Background SNR	4.56E-11	1.30E-07	8.96E-09	8.93E-10
CNR	1.54E-11	1.30E-07	5.99E-09	8.88E-10

Table 4.6. Patient experiment edge preservation results: ANLM has the highest average edge preservation (EP) metrics as a result of insufficient noise suppression. ROVST and LMMSE demonstrate lower average metrics as a result of overcompensation. ACER defines an optimal balance between noise suppression and edge preservation which enhances visualization with the second highest EP metrics.

Case	**ACER**	**ROVST**	**LMMSE**	**ANLM**
1	0.977	0.994	0.982	**1.000**
2	0.936	0.982	0.954	**0.996**
3	0.953	0.875	0.932	**0.979**
4	**0.956**	0.840	0.847	0.954
5	0.846	0.832	0.836	**0.957**
6	0.933	0.881	0.907	**0.980**
7	0.895	0.884	0.890	**0.979**
8	0.971	0.863	0.930	**0.975**
9	0.896	0.861	0.881	**0.963**
10	0.954	0.869	0.903	**0.976**
11	0.923	0.792	0.938	**0.973**
12	0.970	0.867	0.872	**0.981**
13	0.960	0.896	0.902	**0.984**
14	0.985	0.923	0.921	**0.987**
15	0.935	0.838	0.860	**0.969**
16	0.952	0.868	0.868	**0.978**
17	0.973	0.903	0.906	**0.984**
18	0.957	0.986	0.957	**0.999**
19	0.980	0.993	0.981	**1.000**
20	0.974	0.992	0.971	**1.000**
Avg.	0.946	0.897	0.912	**0.981**

required to suppress the noise. This led to overcompensation in other regions where detail is important. Following the conclusions made in the phantom experiment, ROVST and LMMSE led to over suppression of noise and a lower EP measurement. ANLM however, had better EP for all but one case, as a consequence of its insufficient noise compensation. Due to the strong presence of noise in these slices, the Laplacian operator of the EP metric realized noise as edges. The insufficient noise suppression by ANLM resulted in structure preservation in the prostate, however also retained noise in regions of low SNR. This was demonstrated by the lower average background SNR compared to ACER demonstrated in Section 4.7.2. ACER proved to have a suitable balance of noise suppression and EP as a result of the non-stationary unified ERC parametric model used.

The EP analysis is further supported by the visual results shown in Figure 4.4, 4.5 and 4.7. LMMSE and ROVST are able to apply moderate noise suppression in the background regions where signal is low, however nearest the coil the prostate details are difficult to visualize due to overcompensation. ANLM is more effective in retaining the detail within the prostate region however at the cost of retaining the noise farther away from the ERC at high noise levels. ACER strikes an optimal balance between detail preservation within the prostate where signal is higher and effectively suppresses noise in the regions with low signal. This correction allows for improved visibility for diagnosis.

4.7.3 Image analysis and subjective interpretation

To appropriately assess the quality of the noise compensation approaches, a blind subjective scoring system similar to the evaluation system proposed by Walsh *et al.* [77] was used. In this system, the scorers were unaware of which approach was applied on the compensated data presented to them. A central slice from three volumes was selected and evaluated by seven evaluators ranging in experience. They are listed below from most to least experience:

- MH, 16 years of clinical radiology experience with specialization in genitourinary cancers and 11 years of experience interpreting prostate MRI
- LM, 7 years of clinical radiology experience with specialization in cancer imaging
- FK, 5 years of prostate MRI research experience
- HC, 1.5 years of clinical radiology experience
- AM, 1.5 years of clinical imaging research experience

- JK, 2 months of clinical prostate MRI experience
- KC, 50 hours of clinical prostate MRI experience

To collect the subjective scores, the noise-suppressed and uncorrected versions three slices were presented to the evaluators in an unknown and random sequence. Based on the individual slice, they were asked to assess the reconstruction based on the following criteria: contrast, sharpness, lack of noise and fitness for purpose. These criteria can be scored using the following terms: very poor, poor, satisfactory, good or very good. For the sake of our evaluation, we assigned these scores from 1 to 5, with 1 being very poor and 5 being very good. The rank sums (Equation 4.14), median and F-pseudosigma scores (Equation 4.15) across all slices and evaluators were calculated and are shown in Table 4.7, 4.8, 4.9. Histograms of each scoring criterion and the frequency of each score across all evaluators is included in Figure 4.8.

The rank sum, S_R, is the total of all subjective scores by all the evaluators for a particular criterion.

$$S_R = \sum_{i=1}^{N} \sum_{j=1}^{M} S_{ij}, \tag{4.14}$$

where N is the number of evaluators and M is the number of slices evaluators evaluated and S_{ij} are the individual scores of each evaluator for each slice. The total rank sum can then be used to determine whether in general the evaluators decided a particular criterion was high or low for a given approach.

The next metric considered is the F-pseudosigma, F_σ, which is a measurement of variance and is calculated using:

$$F_\sigma = \frac{IQR}{1.349}, \tag{4.15}$$

where IQR is the interquartile range. A smaller F-pseudosigma denotes a more precise score.

Considering the histograms (Figure 4.8), rank sum (Table 4.7), median (Table 4.8) and F-pseudosigma (Table 4.9) metrics for contrast, ACER had the highest rank sum with a median score of satisfactory. It also had the smallest F-pseudosigma which indicates there was little variation between all scores. For the sharpness criterion, it was interesting that

the uncorrected image had the largest rank sum with ANLM having the next highest rank sum. ACER, ANLM and uncorrected tied with the highest median scores of satisfactory however also had the highest F-pseudosigmas indicating large variation in opinion. It was unanimous however that LMMSE had very poor sharpness and was found to be less sharp than the uncorrected slices. For the lack of noise criterion, ACER again had the largest rank sum with a median score of good. All correction approaches had high rank sums and median scores of good however again, F-pseudosigmas hinted at large variance in opinion. This may have been caused by the large number of evaluators and the variance in noise level between cases. Finally, ACER and ANLM had the highest rank sums for fitness for purpose with a median score of satisfactory. LMMSE and ROVST were found to be unfit for the purpose in comparison to uncorrected slices. It is intriguing to point out that evaluators found that the uncorrected slices were just as sufficient for analysis as ACER and ANLM however there was large variance in opinion with large F-pseudosigma scores.

Table 4.7. The rank sum subjective score values (with highest scores shown in bold): ACER has the highest rank sum for contrast and lack of noise.

Scoring Criterion	ACER	ROVST	LMMSE	ANLM	UC
Contrast	**63**	61	47	60	62
Sharpness	58	48	21	65	**68**
Lack of noise	**80**	76	76	72	62
Fitness for purpose	**70**	54	27	**70**	65

Table 4.8. The median subjective score values (with the highest scores shown in bold): ACER and ANLM demonstrated the same median scores as UC except for lack of noise where all approaches improved upon UC.

Scoring Criterion	ACER	ROVST	LMMSE	ANLM	UC
Contrast	**3**	**3**	2	**3**	**3**
Sharpness	**3**	2	1	**3**	**3**
Lack of noise	**4**	**4**	**4**	**4**	3
Fitness for purpose	**3**	2	1	**3**	**3**

Table 4.9. The F-pseudosigma subjective score values (with the lowest scores shown in bold): With the exception of the unanimous decision that LMMSE had poor sharpness, most of the criteria for the approaches had high variance indicating large inconsistencies in opinion implying that personal preference has a large impact upon the approach.

Scoring Criterion	ACER	ROVST	LMMSE	ANLM	UC
Contrast	**0.37**	0.74	0.74	0.74	1.48
Sharpness	0.93	0.74	**0.00**	0.93	0.93
Lack of noise	0.93	0.93	1.48	0.74	**0.19**
Fitness for purpose	0.93	**0.74**	**0.74**	**0.74**	1.48

4.7.4 Visual assessment

Visual results for two different cases are shown in Figure 4.4 and 4.7 for a Hologic rigid ERC and a Medrad inflatable ERC respectively. The results demonstrate ACER's ability to retain prostate detail with effective compensation of background noise using different ERCs with different SNR characteristics. In Figure 4.4, it is evident that LMMSE and ANLM are able to reduce the noise in the background regions however with noise still visibly present. ROVST does a better job at compensating for noise however upon closer inspection of Figure 4.4 in regions specified by Figure 4.5 for a background and prostate region (Figure 4.6) it is apparent that the level of detail is compromised for these approaches. ROVST and LMMSE approaches were unable to preserve the tissue texture within the prostate, demonstrating oversmoothing in the prostate in order to compensate for the high level of noise in the background. In contrast, ANLM was able to retain the detail within the prostate however showed some noise in the background. ACER successfully balances the noise reduction and the detail preservation by incorporating the ERC SNR profile as well as the non-stationary characteristics of the MRI data. Similar conclusions can be made when considering the performance of the approaches for the inflatable ERC case (Figure 4.7). In this example, the ANLM applies insufficient noise compensation and shows evidence of noise. ROVST and LMMSE suppress the noise however at the cost of removing detail in the prostate. Again, ACER exhibits apt noise compensation while retaining tissue texture and details.

4.7.5 Timing analysis

The various MRI compensation approaches were also analyzed based on their computation times. Tests were completed on a 3.10 GHz AMD Athlon(tm) II X3 445 processor with 4.00 GB of RAM. The various approaches were not optimized for timing performance. The timing analysis is shown for the patient data in Table 4.10. The LMMSE approach demonstrated the fastest computation times with an average computation time of 0.13 s while ANLM exhibited the slowest computation time with an average calculation time of 1060 s. The proposed approach, ACER, showed middle range performance with an average computation time of 284 s.

Table 4.10. Computation times for each approach on the real T2 endorectal MRI shown in seconds. Shortest computation times are shown bolded. LMMSE had the shortest average computation time with 0.13 s while ANLM had the longest average computation time with 1060 s.

Case	ACER	ROVST	LMMSE	ANLM
1	370	9.82	**0.17**	1170
2	265	8.22	**0.12**	1090
3	256	8.33	**0.13**	1310
4	270	8.43	**0.13**	1340
5	268	8.47	**0.11**	1310
6	274	8.34	**0.12**	1280
7	299	8.32	**0.12**	1330
8	361	8.43	**0.13**	1330
9	295	8.5	**0.12**	1240
10	285	8.42	**0.12**	1210
11	272	8.31	**0.12**	1210
12	276	7.22	**0.19**	923
13	275	6.99	**0.11**	888
14	274	6.85	**0.12**	848
15	273	7.03	**0.12**	846
16	273	6.99	**0.12**	789
17	272	7.06	**0.14**	871
18	272	7.28	**0.13**	753
19	272	7.34	**0.14**	693
20	273	7.28	**0.12**	690
Avg.	284	7.88	**0.13**	1060

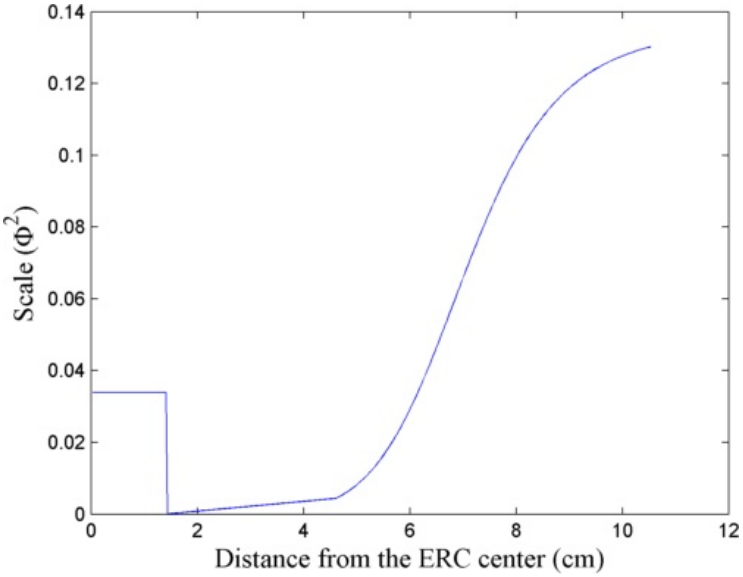

Hologic rigid ERC parametric model profile

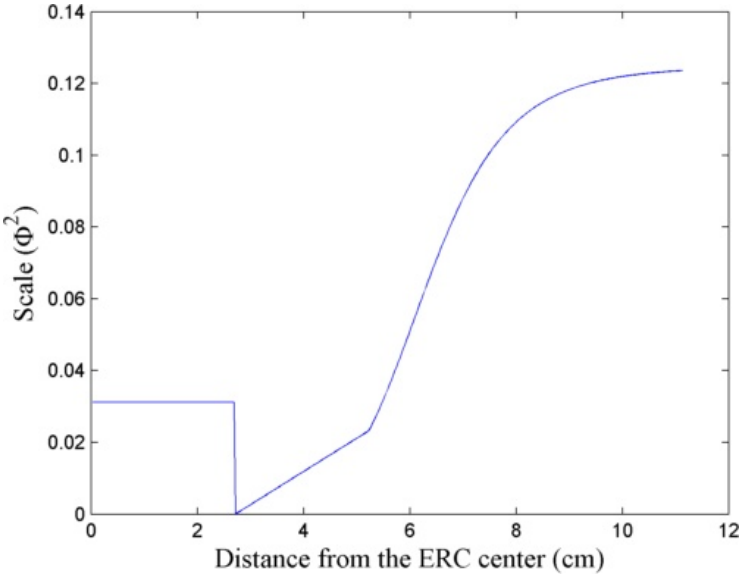

Medrad inflatable ERC parametric model profile

Figure 4.1. The cross-sections of the unified parametric ERC variance models for the rigid Hologic ERC and the inflatable Medrad ERC. The plot shows the profile from the center of the coil and outwards in one direction.

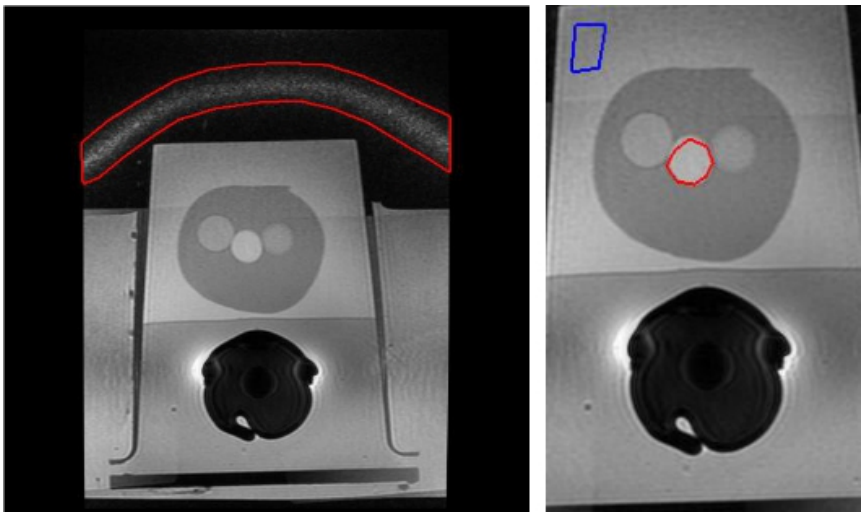

Figure 4.2. Left: Uncorrected uncropped T2 slice. A noise band (red) is present due to PURE correction which amplifies the noise around the cushion used to stabilize the phantom during imaging. Right: Corresponding slice cropped for processing to include only the ROI with selected regions (blue and red) for SNR and CNR calculation on phantom DWI and T2.

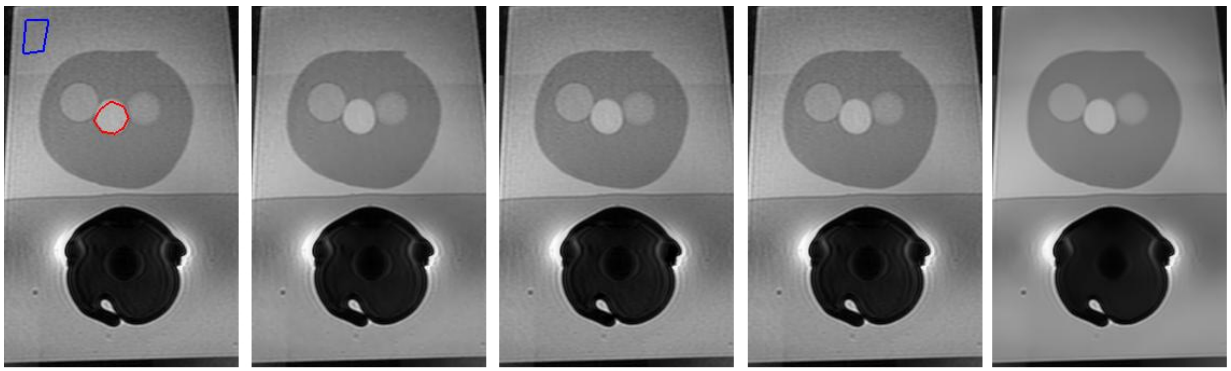

Figure 4.3. Noise suppressed T2 phantom experiment results: A background region (blue) and a prostate region (red) are shown where the SNR and CNR were calculated in the uncorrected (UC) slice. ACER maintains a good balance between noise compensation in smooth regions while retaining edges.

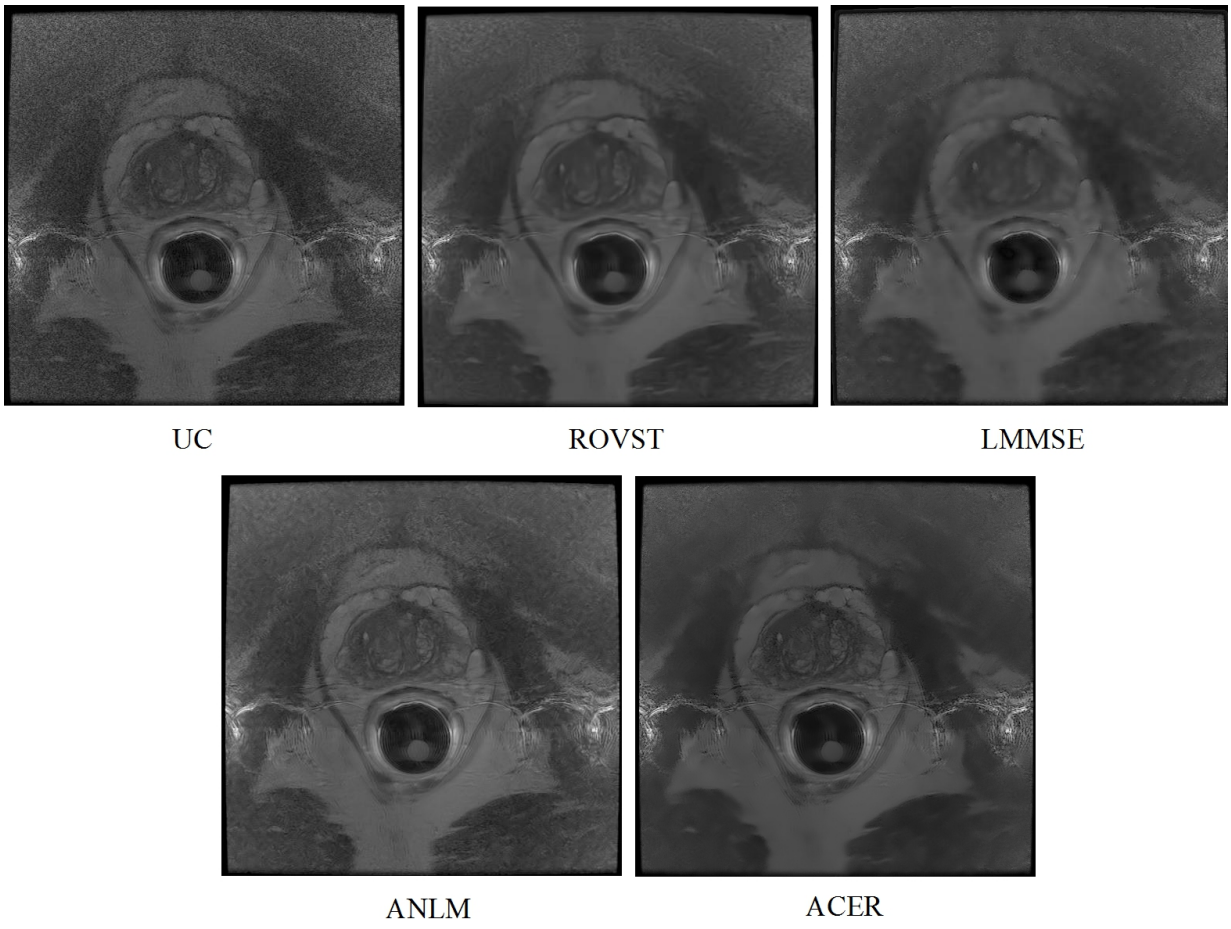

Figure 4.4. Case 12: A central T2 MRI slice from a patient imaged using a Hologic rigid ERC with moderate noise compensated by various approaches. ACER maintains the detail within the prostate while compensating for the background noise.

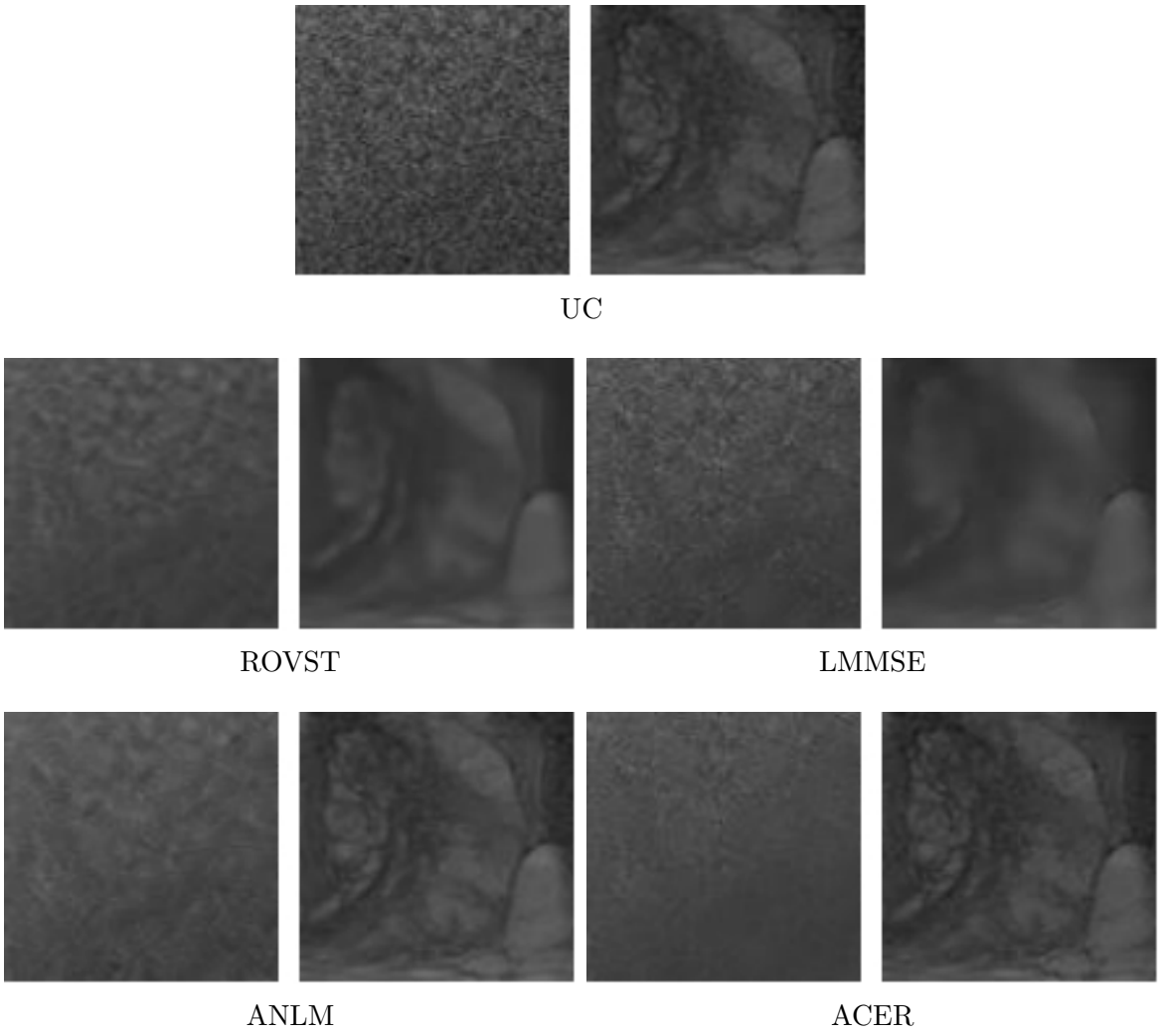

Figure 4.5. Close-up views of background (left) and prostate (right) paired regions for Case 12. The selected regions are shown in Figure 4.6.

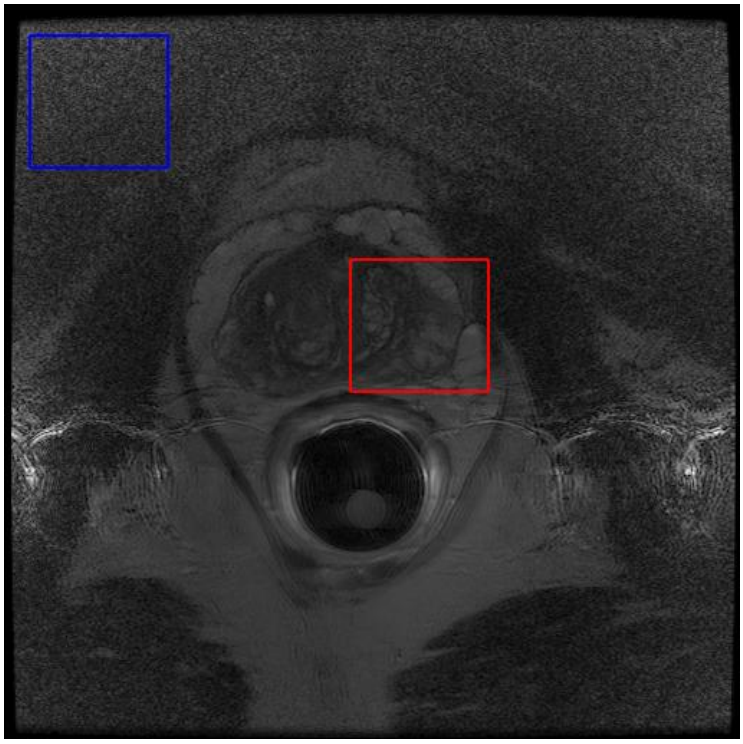

Figure 4.6. Selected background and prostate regions (shown on the uncorrected image) for closer inspection in Figure 4.5.

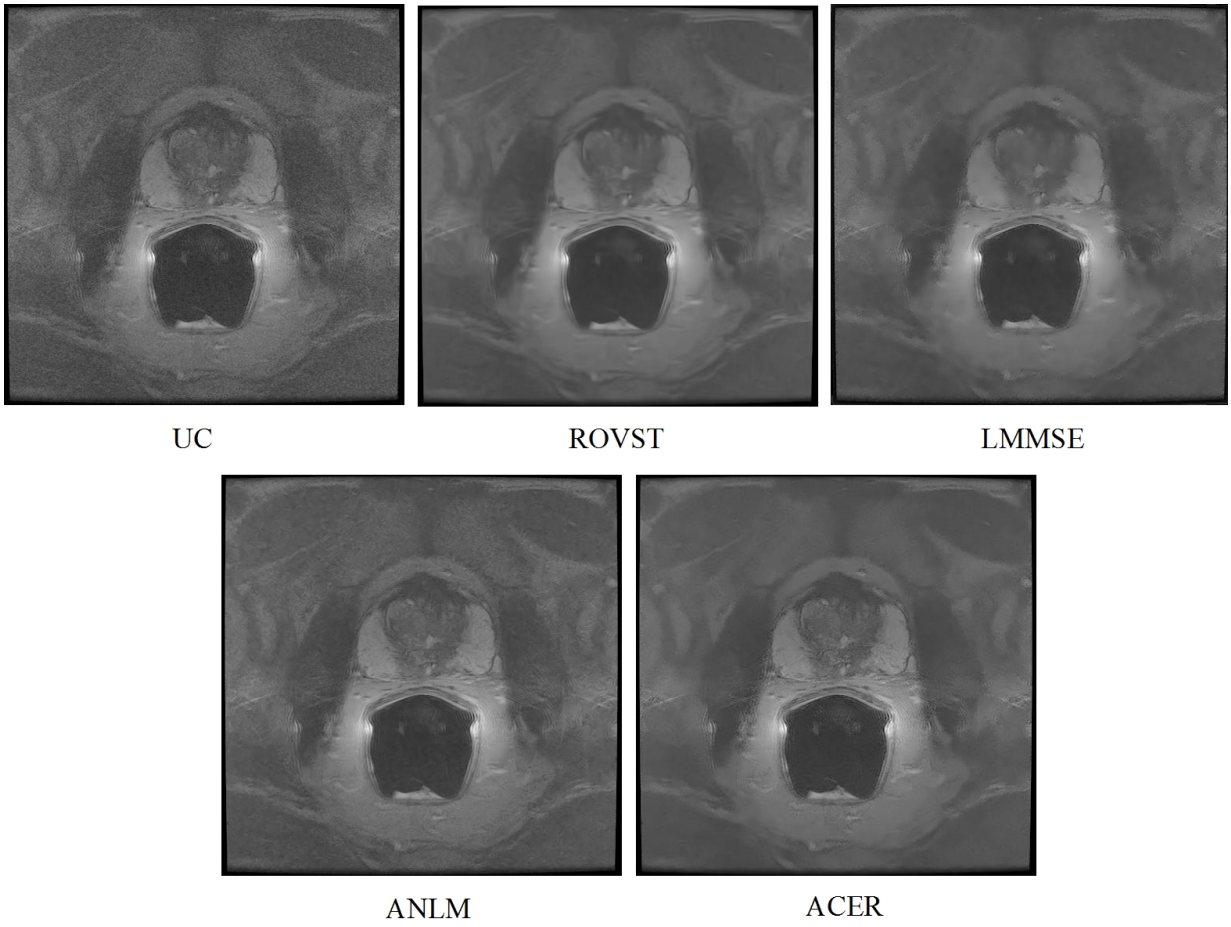

Figure 4.7. Case 3: A central T2 MRI slice from a patient imaged using a Medrad inflatable ERC compensated by various approaches. LMMSE and ROVST suppress noise in the background, consequently blurring details within the prostate. ACER effectively compensates the noise in low signal regions while taking advantage of the high signal near the coil. ANLM maintains similar detail preservation however retains some noise.

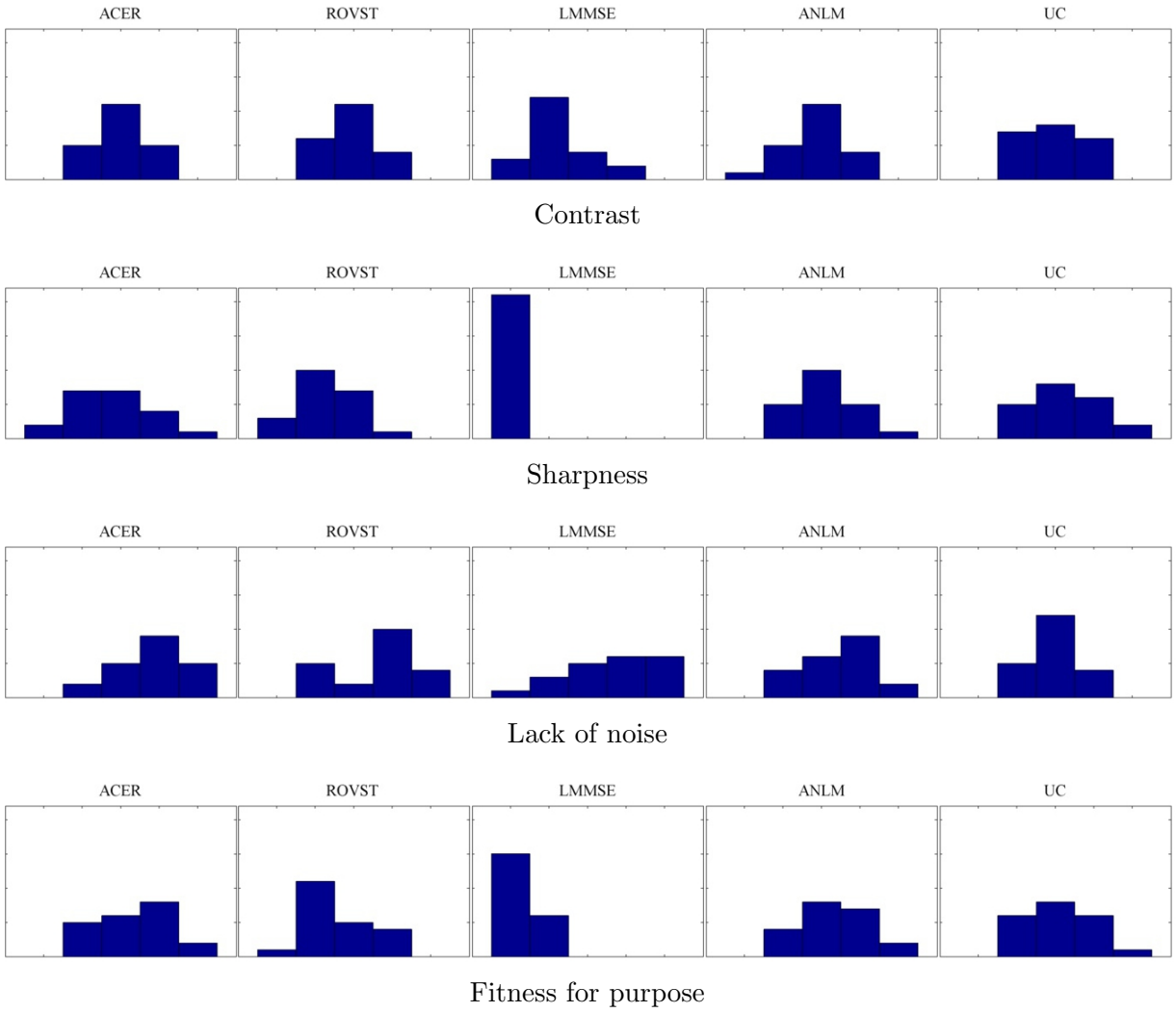

Figure 4.8. Subjective scoring histograms for the compared approaches. The y-axis depicts Frequency (0 to 22) and the x-axis depicts the subjective score (1 to 5).

4.8 Chapter summary

In this chapter, a novel noise compensation approach for coil intensity corrected endorectal MRI images is presented. Adaptive Coil Enhancement Reconstruction (ACER) uses a spatially-adaptive Monte Carlo sampling approach to estimate the Rician-distributed posterior in MRI images to reconstruct the noise compensated image. ACER takes advantage of the known SNR characteristics of an ERC to develop a non-spatial unified ERC parametric model that models the SNR profile presented by the ERC. This allows for effective noise suppression and detail preservation in the prostate. Experimental results using both phantom and patient data showed that ACER provided strong performance in terms of SNR, CNR and edge preservation when compared to a number of existing approaches.

To validate the performance of the proposed approach, it was compared against three other state-of-the-art MRI denoising approaches: ROVST, LMMSE and ANLM using phantom and patient coil intensity corrected endorectal MRI data. The comparison showed that ACER had the most improvement in SNR and CNR in a phantom acquired with DWI and T2 MRI. With patient endorectal T2 MRI, ACER demonstrated the best average improvement of 11.7 dB and 11.2 dB for SNR and CNR respectively over the uncorrected image. It also showed an optimal balance between noise suppression and detail preservation that proved difficult for the compared approaches. As such, ACER provided improved visualization of the prostate which was further supported by subjective scoring and edge preservation analysis. ROVST and LMMSE were able to compensate for moderate noise levels, however, at the cost of smoothing the details within the prostate. ANLM fared better by compensating for the noise and preserving the prostate detail, however, at higher noise levels, it was unable to appropriately compensate for noise.

ACER's improved performance was a result of considering the statistical characteristics of coil intensity corrected MRI data and also the ERC SNR profile. This enabled ACER to take advantage of regions with high SNR and compensate accordingly for regions of low SNR. Also, it was important to consider the non-stationarity of the data, the approaches LMMSE and ROVST considered a single noise variance across the data and as a result led to poor balancing of detail preservation and noise compensation. ANLM's non-local account of the mean enables a more successful correction, however, does not apply this non-local consideration to noise variance.

The encouraging results of ACER's experiments demonstrate the improved visualization of the prostate and completes the final step in the proposed Monte Carlo framework for prostate cancer correction and reconstruction in endorectal multi-parametric MRI. Final conclusions and future work are proposed in the next chapter.

Chapter 5

Conclusion and Future Work

5.1 Summary

In this thesis, a Monte Carlo framework for prostate cancer correction and reconstruction in endorectal multi-parametric MRI is presented. Using importance-weighted Monte Carlo sampling techniques, a two step-process was proposed handling two common challenges in endorectal multi-parametric MRI. The first step handles intensity bias caused by SNR variation due to the endorectal coil. Following this step, noise still persists and becomes non-stationary as a result of the bias correction. The second step then addresses this non-stationary noise for improved visualization of the prostate for easier analysis and detection of prostate cancer.

In Chapter 3, the Monte Carlo bias correction (MCBC) approach was introduced to address intensity bias in endorectal multi-parametric MRI. Using importance-weighted Monte Carlo sampling, a non-parametric estimate of the intensity bias field is computed. With this bias field estimate, it can then be removed from the original image. Comparison against state-of-the-art approaches demonstrated through a series of experiments using synthetic and physical phantoms as well as real patient data that MCBC improves prostate delineation from the background. Moreover it does not introduce artifacts or distort prostate detail. Results showed that an MCBC corrected synthetic phantom had the highest correlation with a non-endorectal T2 image (Table 3.1) and the second lowest variation in a selected region of a physical phantom (Table 3.2). Strong delineation of the prostate from surrounding background was supported by MCBC's highest average Fisher criterion (Table 3.3) and low average probability of error scores when classifying prostate and background tissues (Table 3.4). Computed high b-value DWI generated from MCBC

corrected low b-value DWI also demonstrated improved visualization of tumorous regions by mitigating intensified regions caused by ERCs. Visual assessment also supported these quantitative experiments and proved MCBC diminishes the intensity bias in addition to preserving details which facilitate prostate cancer diagnosis.

Following intensity bias correction through MCBC, noise remains and the second step in the Monte Carlo framework presented in Chapter 4 addresses this. In Chapter 4, adaptive coil enhancement reconstruction (ACER) algorithm uses a spatially-adaptive Monte Carlo sampling approach to estimate the final bias-free, noise-compensated reconstruction. The approach considers the Rician distribution of the MRI data and accounts for the ERC's SNR profile to improve visualization while maintaining critical tissue details. Using a physical phantom, ACER demonstrated the highest background and prostate SNR (Tables 4.1) with the highest average CNR (Tables 4.2). P-value calculations showed the background SNR and CNR metrics were statistically significant with values below 0.05 (Table 4.3). Patient experiments further established the improved SNR in the background with ACER having the highest average background SNR and CNR for twenty cases (Table 4.4). Again, p-value metrics measured for these experiments indicated statistically significant changes from the uncorrected slices (Table 4.5). Edge preservation results showed ACER with the second highest average metrics behind an approach which preserved all the details as well as the noise (Table 4.6). Finally, subjective scoring by seven evaluators ranging in experience, confirmed the visualization improvement with high rank sum (Table 4.7) for all scoring criteria, equivalent or better median scores compared to the uncorrected slice (Table 4.8) and low F-pseudosigma for contrast (Table 4.9). Visual analysis supported these results where ACER aptly suppressed noise in spite of the spatial variation without distorting prostate textures and details enabling for better tissue assessment.

5.2 Future work

The proposed framework has a number of opportunities for future research and extension:

- **Use the proposed framework as a pre-processing step for segmentation.** The proposed Monte Carlo framework presented in this thesis can be utilized as a pre-processing step for segmentation in endorectal multi-parametric MRI. Segmentation of the prostate gland is useful in MRI for prostate cancer grading. By deriving the contour of the prostate from each MRI slice, a volume of segmentations can be used to create a 3D model. The 3D model can also be used for surgical planning. Segmentation in endorectal multi-parametric MRI, however, also suffers from the same

challenges presented in this thesis: intensity bias and noise amplification following intensity bias correction. Using this framework can help improve the segmentation accuracy.

- **Investigate if the ERC SNR profile can be automatically estimated.** Currently, the ERC SNR profile described in the ACER approach (Chapter 4) requires experimental quantification prior to its use. Investigation into whether the underlying MRI data can be used to infer this model would be beneficial for applying the approach to any ERC used in a more automated configuration.

- **Adapt the proposed framework to automatically determine the optimal search space required for posterior estimation.** The importance-weighted Monte Carlo sampling approaches proved effective for posterior estimation, however, empirical testing was required for selecting the most appropriate search spaces. An optimization scheme to select the most suitable search space for estimation would be useful to reduce implementation time and increase the flexibility of the algorithms.

References

[1] Prostate Cancer Canada Network, "Early detection guidelines," 2012. [Online]. Available: http://www.prostatecancer.ca/Prostate-Cancer/About-Prostate-Cancer

[2] National Cancer Institute, "SEER stat fact sheets: Prostate cancer," 2014. [Online]. Available: http://seer.cancer.gov/statfacts/html/prost.html

[3] Canadian Cancer Society, "Prostate cancer statistics," 2014. [Online]. Available: http://www.cancer.ca/en/cancer-information/cancer-type/prostate/statistics/?region=sk

[4] D. Lui, A. Modhafar, J. Glaister, A. Wong, and M. Haider, "Monte Carlo bias field correction in endorectal diffusion imaging," *IEEE Transactions on Biomedical Engineering*, vol. 61, no. 2, pp. 368–380, Feb 2014.

[5] P. R. Carroll, "Early detection of prostate cancer," *Community Oncology*, vol. 7, pp. 25 – 27, 2010.

[6] I. M. Thompson, D. K. Pauler, P. J. Goodman, C. M. Tangen, M. S. Lucia, H. L. Parnes, L. M. Minasian, L. G. Ford, S. M. Lippman, E. D. Crawford *et al.*, "Prevalence of prostate cancer among men with a prostate-specific antigen level $\leq$ 4.0 ng per milliliter," *New England Journal of Medicine*, vol. 350, no. 22, pp. 2239–2246, 2004.

[7] D. Lui, A. Modhafar, A. Wong, and M. Haider, "Monte Carlo-based noise compensation in coil intensity corrected endorectal MRI," 2014, manuscript submitted to IEEE Transactions on Biomedical Engineering for publication.

[8] H. Beerlage, R. Aarnink, E. T. Ruijter, J. Witjes, H. Wijkstra, C. Van De Kaa, F. Debruyne, and J. de la Rosette, "Correlation of transrectal ultrasound, computer analysis of transrectal ultrasound and histopathology of radical prostatectomy specimen." *Prostate Cancer & Prostatic Diseases*, vol. 4, no. 1, 2001.

[9] V. Khoo, A. Padhani, S. Tanner, D. Finnigan, M. Leach, and D. Dearnaley, "Comparison of MRI with CT for the radiotherapy planning of prostate cancer: a feasibility study." *The British Journal of Radiology*, vol. 72, no. 858, pp. 590–597, 1999.

[10] M. Debois, R. Oyen, F. Maes, G. Verswijvel, G. Gatti, H. Bosmans, M. Feron, E. Bellon, G. Kutcher, H. Van Poppel *et al.*, "The contribution of magnetic resonance imaging to the three-dimensional treatment planning of localized prostate cancer," *International Journal of Radiation Oncology Biology Physics*, vol. 45, no. 4, pp. 857–865, 1999.

[11] N. Desouza, S. Reinsberg, E. Scurr, J. Brewster, and G. Payne, "Magnetic resonance imaging in prostate cancer: the value of apparent diffusion coefficients for identifying malignant nodules," *The British Journal of Radiology*, vol. 80, pp. 90–95, 2007.

[12] K. Hosseinzadeh and S. D. Schwarz, "Endorectal diffusion-weighted imaging in prostate cancer to differentiate malignant and benign peripheral zone tissue," *Journal of Magnetic Resonance Imaging*, vol. 20, pp. 654–661, 2004.

[13] M. A. Haider, T. H. van der Kwast, J. Tanguay, A. J. Evans, A.-T. Hashmi, G. Lockwood, and J. Trachtenberg, "Combined T2-weighted and diffusion-weighted MRI for localization of prostate cancer," *American Journal of Roentgenology*, vol. 189, no. 2, pp. 323–328, 2007.

[14] D. Koh and A. Padhani, "Diffusion weighted MRI a new functional clinical technique for tumour imaging," *The British Journal of Radiology*, vol. 79, pp. 633–635, 2006.

[15] J. Glaister, A. Cameron, A. Wong, and M. Haider, "Quantitative investigative analysis of tumour separability in the prostate gland using ultra-high b-value computed diffusion imaging," in *2012 Annual International Conference of the IEEE, Engineering in Medicine and Biology Society (EMBC)*, 2012, pp. 420–423.

[16] A. B. Rosenkrantz, N. Hindman, H. Chandarana, F. ming Deng, J. S. Babb, S. Taneja, and C. Geppert, "Computed diffusion-weighted imaging of the prostate at 3T: Impact on image quality and tumor detection," in *21st Annual Meeting and Exhibition, International Society for Magnetic Resonance in Medicine (ISMRM)*, 2013, p. 94.

[17] C. K. Kim, B. K. Park, and B. Kim, "High b-value diffusion-weighted imaging at 3T to detect prostate cancer: Comparisons between b-values of 1,000 and 2,000 s/mm^2," *American Journal of Roentgenology*, vol. 194, no. 1, pp. W33–W37, 2010.

[18] T. Metens, D. Miranda, J. Absil, and C. Matos, "What is the optimal b-value in diffusion-weighted MR imaging to depict prostate cancer at 3T?" *European Radiology*, vol. 22, no. 3, pp. 703–709, 2012.

[19] M. A. Haider, T. H. van der Kwast, J. Tanguay, A. J. Evans, A.-T. Hashmi, G. Lockwood, and J. Trachtenberg, "Combined T2-weighted and diffusion-weighted MRI for localization of prostate cancer," *American Journal of Roentgenology*, vol. 189, no. 2, pp. 323–328, 2007.

[20] B. Turkbey, M. J. Merino, E. C. Gallardo, V. Shah, O. Aras, M. Bernardo, E. Mena, D. Daar, A. R. Rastinehad, W. M. Linehan *et al.*, "Comparison of endorectal coil and nonendorectal coil T2W and diffusion-weighted MRI at 3 Tesla for localizing prostate cancer: Correlation with whole-mount histopathology," *Journal of Magnetic Resonance Imaging*, vol. 39, no. 6, pp. 1443–1448, 2014.

[21] J. Sosna, I. Pedrosa, W. C. Dewolf, H. Mahallati, R. E. Lenkinski, and N. M. Rofsky, "MR imaging of the prostate at 3 Tesla: comparison of an external phased-array coil to imaging with an endorectal coil at 1.5 Tesla," *Academic Radiology*, vol. 11, no. 8, pp. 857–862, 2004.

[22] D. Beyersdorff, K. Taymoorian, T. Knösel, D. Schnorr, R. Felix, B. Hamm, and H. Bruhn, "MRI of prostate cancer at 1.5 and 3.0 T: comparison of image quality in tumor detection and staging," *American Journal of Roentgenology*, vol. 185, no. 5, pp. 1214–1220, 2005.

[23] N. D. Gelber, R. L. Ragland, and J. R. Knorr, "Surface coil MR imaging: utility of image intensity correction filter." *American Journal of Roentgenology*, vol. 162, no. 3, pp. 695–697, 1994.

[24] G. P. Liney, L. W. Turnbull, and A. J. Knowles, "A simple method for the correction of endorectal surface coil inhomogeneity in prostate imaging," *Journal of Magnetic Resonance Imaging*, vol. 8, no. 4, pp. 994–997, 1998.

[25] A. Wong and A. K. Mishra, "Quasi-Monte Carlo estimation approach for denoising MRI data based on regional statistics," *IEEE Transactions on Biomedical Engineering*, vol. 58, no. 4, pp. 1076–1083, 2011.

[26] H. M. Golshan, R. P. Hasanzadeh, and S. C. Yousefzadeh, "An MRI denoising method using image data redundancy and local SNR estimation," *Magnetic Resonance Imaging*, vol. 31, no. 7, pp. 1206–1217, 2013.

[27] J. V. Manjón, N. A. Thacker, J. J. Lull, G. Garcia-Martí, L. Martí-Bonmatí, and M. Robles, "Multicomponent MR image denoising," *Journal of Biomedical Imaging*, vol. 2009, p. 18, 2009.

[28] A. Foi, "Noise estimation and removal in MR imaging: the variance-stabilization approach," in *2011 IEEE International Symposium on Biomedical Imaging: From Nano to Macro*. IEEE, 2011, pp. 1809–1814.

[29] H. Gudbjartsson and S. Patz, "The Rician distribution of noisy MRI data," *Magnetic Resonance in Medicine*, vol. 34, no. 6, pp. 910–914, 1995.

[30] J. Sijbers and A. Den Dekker, "Maximum likelihood estimation of signal amplitude and noise variance from MR data," *Magnetic Resonance in Medicine*, vol. 51, no. 3, pp. 586–594, 2004.

[31] N. Wiest-Daesslé, S. Prima, P. Coupé, S. P. Morrissey, and C. Barillot, "Rician noise removal by non-local means filtering for low signal-to-noise ratio MRI: Applications to DT-MRI," in *Medical Image Computing and Computer-Assisted Intervention–MICCAI 2008*. Springer, 2008, pp. 171–179.

[32] L. He and R. Greenshields Ian, "A nonlocal maximum likelihood estimation method for Rician noise reduction in MR images," *IEEE Transactions on Medical Imaging*, vol. 28, no. 2, pp. 165–172, 2009.

[33] B. H. Brinkmann, A. Manduca, and R. A. Robb, "Optimized homomorphic unsharp masking for MR grayscale inhomogeneity correction," *IEEE Transactions on Medical Imaging*, vol. 17, pp. 161–171, 1998.

[34] L. Axel, J. Costantini, and J. Listerud, "Intensity correction in surface-coil MR imaging," *American Journal of Roentgenology*, vol. 148, no. 2, pp. 418–420, 1987.

[35] U. Vovk, F. Pernus, and B. Likar, "A review of methods for correction of intensity inhomogeneity in MRI," *IEEE Transactions on Medical Imaging*, vol. 26, pp. 405–421, 2007.

[36] B. Belaroussia, J. Millesb, S. Carmec, Y. M. Zhua, and H. Benoit-Cattina, "Intensity non-uniformity correction in MRI: Existing methods and their validation," *Medical Image Analysis*, vol. 10, pp. 234–246, 2006.

[37] G. B. Avinash and G. E. Company, "Method for correcting inhomogeneity of spatial intensity in an acquired MR image," US Patent US59 437 433 A, Aug 24, 1999.

[38] G. P. Liney, L. W. Turnbull, and A. J. Knowles, "A simple method for the correction of endorectal surface coil inhomogeneity in prostate imaging," *Journal of Magnetic Resonance Imaging*, vol. 8, no. 4, pp. 994–997, 1998.

[39] A. Koivula, J. Alakuijala, and O. Tervonen, "Image feature based automatic correction of low-frequency spatial intensity variations in MR images," *Magnetic Resonance Imaging*, vol. 15, no. 10, pp. 1167–1175, 1997.

[40] L. Zhou, Y. Zhu, C. Bergot, A.-M. Laval-Jeantet, V. Bousson, J.-D. Laredo, and M. Laval-Jeantet, "A method of radio-frequency inhomogeneity correction for brain tissue segmentation in MRI," *Computerized Medical Imaging and Graphics*, vol. 25, no. 5, pp. 379–389, 2001.

[41] B. M. Dawant, A. P. Zijdenbos, and R. A. Margolin, "Correction of intensity variations in MR images for computer-aided tissue classification," *IEEE Transactions on Medical Imaging*, vol. 12, pp. 770–781, 1993.

[42] C. Hui, Y. X. Zhou, and P. Narayana, "A fast algorithm for calculation of inhomogeneity gradient in MRI data," *Magnetic Resonance Imaging*, vol. 32, no. 5, pp. 1197–1208, Nov 2010.

[43] S. K. Lee and M. W. Vannier, "Post-acquisition correction of MR inhomogeneities," *Magnetic Resonance in Medicine*, vol. 36, no. 2, pp. 275–286, 1996.

[44] D. L. Pham and J. L. Prince, "An adaptive fuzzy C-means algorithm for image segmentation in the presence of intensity inhomogeneities," *Pattern Recognition Letters*, vol. 20, no. 1, pp. 57–68, 1999.

[45] K. Van Leemput, F. Maes, D. Vandermeulen, and P. Suetens, "Automated model-based bias field correction of MR images of the brain," *IEEE Transactions on Medical Imaging*, vol. 18, no. 10, pp. 885–896, 1999.

[46] W. M. Wells III, W. E. L. Grimson, R. Kikinis, and F. A. Jolesz, "Adaptive segmentation of MRI data," *IEEE Transactions on Medical Imaging*, vol. 15, no. 4, pp. 429–442, 1996.

[47] J. G. Sled, A. P. Zijdenbos, and A. C. Evans, "A nonparametric method for automatic correction of intensity nonuniformity in MRI data," *IEEE Transactions on Medical Imaging*, vol. 17, no. 1, p. 8797, 1998.

[48] R. P. Velthuizen, J. J. Heine, A. B. Cantor, H. Lin, L. M. Fletcher, and L. P. Clarke, "Review and evaluation of MRI nonuniformity corrections for brain tumor response measurements," *Medical Physics*, vol. 25, no. 9, pp. 1655–1666, 1998.

[49] S.-H. Lai and M. Fang, "A new variational shape-from-orientation approach to correcting intensity inhomogeneities in magnetic resonance images," *Medical Image Analysis*, vol. 3, pp. 409–424, 1999.

[50] Z. Hou, "A review on MR image intensity inhomogeneity correction," *International Journal of Biomedical Imaging*, vol. 2006, 2006.

[51] V. Varghees, M. Manikandan, and R. Gini, "Adaptive MRI image denoising using total-variation and local noise estimation," in *2012 International Conference on Advances in Engineering, Science and Management (ICAESM)*. IEEE, 2012, pp. 506–511.

[52] A. Pizurica, W. Philips, I. Lemahieu, and M. Acheroy, "A versatile wavelet domain noise filtration technique for medical imaging," *IEEE Transactions on Medical Imaging*, vol. 22, no. 3, pp. 323–331, 2003.

[53] P. Coupé, J. V. Manjón, M. Robles, L. D. Collins *et al.*, "Adaptive multiresolution non-local means filter for 3D MR image denoising," *IET Image Processing*, 2011.

[54] C. S. Anand and J. S. Sahambi, "Wavelet domain non-linear filtering for MRI denoising," *Magnetic Resonance Imaging*, vol. 28, no. 6, pp. 842–861, 2010.

[55] Y. Wang, X. Che, and S. Ma, "Nonlinear filtering based on 3D wavelet transform for MRI denoising," *EURASIP Journal on Advances in Signal Processing*, vol. 2012, no. 1, pp. 1–14, 2012.

[56] A. Martin, J.-F. Garamendi, and E. Schiavi, "MRI TV-Rician denoising," in *Biomedical Engineering Systems and Technologies*. Springer, 2013, pp. 255–268.

[57] R. D. Nowak, "Wavelet-based Rician noise removal for magnetic resonance imaging," *IEEE Transactions on Image Processing*, vol. 8, no. 10, pp. 1408–1419, 1999.

[58] S. L. Keeling, M. Hintermüller, F. Knoll, D. Kraft, and A. Laurain, "A total variation based approach to correcting surface coil magnetic resonance images," *Applied Mathematics and Computation*, vol. 218, no. 2, pp. 219–232, 2011.

[59] S. Aja-Fernández, C. Alberola-López, and C.-F. Westin, "Noise and signal estimation in magnitude MRI and Rician distributed images: a LMMSE approach," *IEEE Transactions on Image Processing*, vol. 17, no. 8, pp. 1383–1398, 2008.

[60] P. Kellman and A. Arai, "Surface coil intensity correction for phase sensitive inversion recovery delayed enhancement of myocardial infarction improves image appearance," vol. 15, 2007.

[61] A. Buades, B. Coll, and J.-M. Morel, "A non-local algorithm for image denoising," in *IEEE Computer Society Conference on Computer Vision and Pattern Recognition*, vol. 2. IEEE, 2005, pp. 60–65.

[62] Y. Zhan, M. Ding, F. Xiao, and X. Zhang, "An improved non-local means filter for image denoising," in *Intelligent Computation and Bio-Medical Instrumentation (ICBMI), 2011 International Conference on*. IEEE, 2011, pp. 31–34.

[63] M.-H. Chen, "Importance-weighted marginal Bayesian posterior density estimation," *Journal of the American Statistical Association*, vol. 89, pp. 818–824, 1994.

[64] M. N. Ahmed, S. M. Yamany, N. Mohamed, A. A. Farag, and T. Moriarty, "A modified fuzzy C-means algorithm for bias field estimation and segmentation of MRI data," *IEEE Transactions on Medical Imaging*, vol. 21, pp. 193–199, 2002.

[65] Y. Zheng, M. Grossman, S. P. Awate, and J. C. Gee, "Automatic correction of intensity nonuniformity from sparseness of gradient distribution in medical images," in *Medical Image Computing and Computer-Assisted Intervention–MICCAI 2009*. Springer, 2009, pp. 852–859.

[66] C. Li, R. Huang, Z. Ding, J. C. Gatenby, D. N. Metaxas, and J. C. Gore, "A level set method for image segmentation in the presence of intensity inhomogeneities with application to MRI," *IEEE Transactions on Image Processing*, vol. 20, pp. 2007–2016, 2011.

[67] O. Salvado, C. Hillenbrand, S. Zhang, and D. L. Wilson, "Method to correct intensity inhomogeneity in MR images for atherosclerosis characterization," *IEEE Transactions on Medical Imaging*, vol. 25, no. 5, pp. 539 – 552, 2006.

[68] D.-J. Kroon, "Bias field corrected fuzzy c-means," 2009. [Online]. Available: https://www.mathworks.com/matlabcentral/fileexchange/25712-bias-field-corrected-fuzzy-c-means

[69] P. Fieguth, *Statistical image processing and multidimensional modeling.* Springer, 2010.

[70] A. Wong, A. Mishra, W. Zhang, P. Fieguth, and D. A. Clausi, "Stochastic image denoising based on markov-chain monte carlo sampling," *Signal Processing*, vol. 91, no. 8, pp. 2112–2120, 2011.

[71] P. Milanfar, "A tour of modern image filtering: new insights and methods, both practical and theoretical," *Signal Processing Magazine, IEEE*, vol. 30, no. 1, pp. 106–128, 2013.

[72] M.-H. Chen, "Importance-weighted marginal Bayesian posterior density estimation," *Journal of the American Statistical Association*, vol. 89, pp. 818–824, 1994.

[73] N. Venugopal, A. Krieger, H. Jeufack, K. Bradshaw, B. McCurdy, and L. Ryner, "Signal characterization of a novel two-channel rigid endorectal coil for MR imaging of the prostate," in *International Society for Magnetic Resonance in Medicine Proceedings.* ISMRM, 2010.

[74] S. M. Noworolski, J. C. Crane, D. B. Vigneron, and J. Kurhanewicz, "A clinical comparison of rigid and inflatable endorectal-coil probes for MRI and 3D MR spectroscopic imaging (MRSI) of the prostate," *Journal of Magnetic Resonance Imaging*, vol. 27, no. 5, pp. 1077–1082, 2008.

[75] C. Arteaga de Castro, B. van den Bergen, P. Luijten, U. van der Heide, M. van Vulpen, and D. Klomp, "Improving SNR and B1 transmit field for an endorectal coil in 7 T MRI and MRS of prostate cancer," *Magnetic Resonance in Medicine*, vol. 68, no. 1, pp. 311–318, 2012.

[76] F. Sattar, L. Floreby, G. Salomonsson, and B. Lovstrom, "Image enhancement based on a nonlinear multiscale method," *IEEE Transactions on Image Processing*, vol. 6, pp. 888–895, 1997.

[77] C. Walsh, A. Dowling, A. Meade, and J. Malone, "Subjective and objective measures of image quality in digital fluoroscopy," *Radiation protection dosimetry*, vol. 117, no. 1-3, pp. 34–37, 2005.